



UNIVERSIDAD MIGUEL
HERNÁNDEZ

*Efecto del método de procesado sobre la
microestructura y bioactividad de andamios
eutectoides dentro del sistema*

$3CaOP_2O_5-2CaOSiO_2$

Carlos Navalón Donat

Directora: Piedad. N de Aza Moya.

Co-directora: Patricia Mazón Canales.

Programa de Doctorado en Bioingeniería

Elche, 2020

INSTITUTO DE BIOINGENERÍA

INDICIOS DE CALIDAD

La tesis doctoral titulada “*Efecto del método de procesado sobre la microestructura y bioactividad de andamios eutectoides dentro del sistema $3CaOP_2O_5-2CaOSiO_2$* ”, realizada por D. CARLOS NAVALON DONAT, con DNI: 48602167Q, bajo la dirección de las profesoras Piedad N. De Aza Moya y Patricia Mazón Canales, se presenta bajo la modalidad de Tesis por compendio de publicaciones con los siguientes índices de calidad según el Campo de la ANEP de Ciencia y Tecnología de Materiales.

Publicaciones Científicas:

C. Navalón, P. Mazón, P.N. De Aza. Eutectoid dicalcium silicate-Nurse’s A ceramic scaffold: processing and in vitro bioactivity.
Ceramic International.45, 21716-21724 (2019).
DOI: 10.1016/j.ceramint.2019.07.172
Factor de Impacto (2018): 3.450
Puesto que ocupa/Nº de revistas en su área (2018): materials science, ceramics : 2/28

C. Navalón, P. Ros-Tárraga, A. Murciano, P. Velásquez, P Mazón, P.N. De Aza. Easy manufacture of 3D ceramic scaffolds by the foam replica technique combined with sol-gel or ceramic slurry.
Ceramic International 45, 18338-18346 (2019).
DOI:10.1016/j.ceramint.2019.06.048
Factor de Impacto (2018): 3.450
Puesto que ocupa/Nº de revistas en su área (2018): materials science, ceramics 2/28



Programa de Doctorado en Bioingeniería

Los abajo firmantes, Piedad N. De Aza Moya, Catedrática de Ciencia de Materiales e Ingeniería Metalúrgica y Directora del Grupo Ciencia de Materiales de la Universidad Miguel Hernández de Elche, y Patricia Mazón Canales, Profesora Contratada Doctor de Ciencia de Materiales e Ingeniería Metalúrgica de la misma Universidad.

INFORMAN:

Que la memoria presentada para optar al grado de Doctor por la Universidad Miguel Hernández de Elche por D. CARLOS NAVALON DONAT, con DNI: 48602167Q, titulada *“Efecto del método de procesado sobre la microestructura y bioactividad de andamios eutectoides dentro del sistema $3CaOP_2O_5-2CaOSiO_2$ ”*, ha sido realizada bajo nuestra dirección.

Que han revisado los contenidos científicos y los aspectos formales del trabajo y dan su conformidad para su presentación a la Comisión de Doctorado de la Universidad Miguel Hernández de Elche.

Y para que así conste, y a los efectos oportunos, firmamos el presente documento en Elche a 20 de abril de 2020

Fdo. Piedad N. De Aza Moya

Fdo. Patricia Mazón Canales



Programa de Doctorado en Bioingeniería

Piedad N. De Aza Moya, Coordinadora del Programa de Doctorado en Bioingeniería de la Universidad Miguel Hernández de Elche por Resolución Rectoral 3120/19, de 09 de diciembre de 2019

INFORMA

Que la tesis doctoral titulada “*Efecto del método de procesado sobre la microestructura y bioactividad de andamios eutectoides dentro del sistema $3CaOP_2O_5-2CaOSiO_2$* ”, ha sido realizada por D. CARLOS NAVALON DONAT, con DNI: 48602167Q, bajo la dirección de las profesoras Piedad N. De Aza Moya y Patricia Mazón Canales, y da su conformidad para que sea presentada a la Comisión de Doctorado de la Universidad Miguel Hernández.

Y para que así conste, y a los efectos oportunos, firma el presente documento en Elche a 20 de abril de 2020

Profesora Piedad N. De Aza Moya.
Coordinadora del Programa de Doctorado en Bioingeniería

AGRADECIMIENTOS

En primer lugar, agradecer a mi directora de tesis Piedad. N de Aza Moya, por haberme dado la oportunidad de iniciar mi carrera profesional en el campo de la investigación y haberme permitido desarrollar este trabajo en el que he ido disfrutando cada vez más y he ido adquiriendo experiencia en un campo que, a priori, no poseía conocimientos previos. Gracias por su ayuda, confianza, flexibilidad y paciencia. Pero, sobre todo, gracias por las enseñanzas transmitidas y las oportunidades que me ha brindado para crecer tanto a nivel profesional, como personal.

A mi co-directora de tesis Patricia Mazón Canales, por haber sido mi primera toma de contacto en el laboratorio. Por haberme escuchado siempre con paciencia. Por haberme guiado en el laboratorio de forma organizada y segura, permitiéndome conseguir buenos resultados en poco tiempo, así como por su atenta ayuda y sus sabios consejos.

A Pablo Velásquez, por haberme enseñado más profundamente, el funcionamiento y el mantenimiento de todos los instrumentos del laboratorio necesarios para desarrollar mi tesis, así como haberme ayudado a manejar y comprender todos los programas informáticos necesarios para analizar los resultados obtenidos.

A Angel Murciano, por haberme enseñado todo lo que necesitaba saber sobre el campo del Sol-gel, desde su preparación hasta sus múltiples aplicaciones. Por haberme transmitido esa pasión y dedicación a la investigación, que tanto le caracteriza. Por haber compartido conmigo su entusiasmo por la gastronomía y su gran afición por los vinos, descubriéndome un gran campo que experimentar.

A Patricia Ross, por todos los favores que me ha hecho para poder adquirir resultados, por su gran capacidad organizativa y resolutiva que nos ayudó a cuadrar la estancia en Murcia, por haberme ayudado a realizar todos los ensayos celulares *in vitro* que he realizado durante este trabajo, por tener paciencia a la hora de enseñarme las técnicas necesarias para desarrollar dichos ensayos, y, sobre todo, por esas quedadas fuera del ámbito laboral donde compartíamos, risas, momentos y resolvíamos el mundo.

A Nayarit Mata y Anabel Diaz, mis dos latinas. Agradecerles su constante e incondicional ayuda y apoyo, por haber estado siempre a mi lado en los momentos más difíciles, por tranquilizarme en momentos tensos, por la cantidad de consejos que me han regalado, no solo en el ámbito profesional, sino también en el personal, por transmitirme

esa dedicación, perseverancia y alegría que tanto las caracteriza. Sin ellas, estos años no hubiesen sido lo mismo.

Al resto de compañeros que han coincidido conmigo en el laboratorio: Laura, Sergio, Paula, Mariano, Ana, Carmen y Laura, por vuestra valiosa compañía y apoyo. A todos ellos, gracias por tantos buenos momentos y por aprender siempre algo nuevo de vosotros.

A mis compañeros de piso, todos científicos, María, Lupita y Julio, por haberme entendido y ayudado siempre que lo he necesitado. Doy gracias por haberme cruzado con vosotros en esta etapa, que hayais sido vosotros las personas con las que he compartido infinidad de momentos inolvidables, así como formar una amistad sincera y duradera.

A mi novia Paula Pla, por ser un pilar fundamental en mi vida, y sobre todo en estos años de tesis, por ser una persona maravillosa que a pesar de la distancia me, ha acompañado a lo largo del camino, así como todo el esfuerzo que ha realizado para comprender mi situación.

A mi familia, que a pesar de ser pequeña es lo mas grande que tengo en el mundo. Por su amor incondicional, por su apoyo en los momentos difíciles y por orientarme correctamente. Gracias por todo, por la educación que he recibido, y por hacerme crecer a nivel personal y profesional.

ÍNDICE

1.	INTRODUCCIÓN	1
1.1.	Biomateriales y su clasificación.	2
1.2.	Ingeniería de Tejidos y Biocerámicas.....	4
1.3.	Diagrama de fases aplicados al diseño de biomateriales.	7
1.3.1.	Biomateriales en el sistema $\text{Ca}_2\text{SiO}_4\text{-Ca}_3(\text{PO}_4)_2$	8
1.3.2.	Silicato dicálcico: C_2S (Ca_2SiO_4)	9
1.3.3.	Fosfato tricálcico: TCP ($\text{Ca}_3(\text{PO}_4)_2$).....	9
2.	OBJETIVOS	11
3.	MATERIALES Y MÉTODOS	13
3.1.	Andamios 3D porosos en Barbotina.	13
3.2.	Andamios 3D porosos en Sol-Gel.	13
3.3.	Bioactividad	14
4.	RESULTADOS.	15
4.1.	Andamios 3D porosos en Barbotina.	15
4.2.	Andamios 3D porosos en Sol-Gel	16
5.	DISCUSIÓN.	19
6.	CONCLUSIONES Y PROYECCIONES FUTURAS.....	25
6.1	Conclusiones.....	25
6.2	Proyecciones Futuras.	26
7.	BIBLIOGRAFÍA.	27
8.	ANEXO: COMPENDIO DE ARTICULOS.....	33
8.1.	Artículo 1.....	35
8.2.	Artículo 2.....	45

ABREVIATURAS y FÓRMULAS QUÍMICAS

BR: Barbotina.

β -Cristobalita: SiO₂ (Alta temperatura).

β -Tridimita: SiO₂ (Ultra-Alta temperatura).

CMM: Células Madre Mesenquimales.

C₂S: Silicato Dicálcico. (Ca₂SiO₄).

CHA: Carbo-Hidroxiapatito.

DRX/XRD: Difracción de Rayos X.

FCB: Fosfato de Calcio Bifásico.

HA: Hidroxiapatito.

ICP-OES: Espectrometría de Emisión Óptica de Plasma Acoplado Inductivamente.

IRTF/FTIR: Espectroscopia infrarroja con Transformada de Fourier.

MEB/SEM: Microscopía Electrónica de Barrido.

Nurse' A: 7CaO·P₂O₅·SiO₂

OMS: Organización Mundial de la Salud.

Pirofosfato: Ca₂P₂O₇.

PU: Esponjas de Poliuretano.

R: Solución Sólida de α' -TCP y α -C₂S.

REP: Réplica de Esponja Polimérica.

SFA/SBF: Suero Fisiológico Artificial.

SG: Sol-Gel.

TCP: Fosfato Tricálcico (Ca₃(PO₄)₂).

TEP: Tetra-Etil-Ortofosfato.

TEOS: Tetra-Etil-Ortosilicato.

ABSTRACT

The increase in life expectancy in a population also leads to its aging, thus increasing the probability of suffering diseases related to bone tissue.

Therefore, the development of biomaterials destined to bone tissue regeneration is necessary. In this thesis, it is proposed to obtain ceramic materials, within the $\text{Ca}_2\text{SiO}_4\text{-Ca}_3(\text{PO}_4)_2$ system, using the Polymer Sponge Replica method (REP) by immersing a polyurethane (PU) sponge in a Sol-gel suspension (SG) and another one from Slurry (BR), followed by a thermal treatment in order to obtain ceramics with a porous 3D structure. Subsequently, the physical-chemical, mineralogical, macro and microstructural characterization of the previously obtained materials will be carried out, as well as their bioactivity evaluation through *in vitro* tests in simulated body fluid (SFA) to study their possible application in bone tissue regeneration.

The characterization of the materials obtained by both methods has been carried out by different techniques, such as XRD, SEM, ATR-FTIR and Hg Porosimetry. The results indicate the scaffolds acquired by SG and BR had similarities at the macrostructure level. However, they present differences in terms of the phases present, microporosity and microstructure.

The scaffolds have an open porosity (~95) whose pore size ranges from 300-600 μm . However, significant differences have been found in relation to microporosity, being 12.83% and 48.9% in the BR and SG scaffolds, respectively. Regarding the mineralogical composition, the BR scaffolds are biphasic due to the presence of the C_2S and Nurse's A phases, while the SG scaffolds are multiphasic because they present several minority phases and C_2S and TCP as majority ones. The results show a lamellar microstructure of alternating layers of C_2S and Nurse's A for BR scaffolds, whereas SG scaffolds present globular microstructure generated by an agglomeration of particles which have lost their identity and have grown cylindrically.

The bioactivity evaluation of the 3D scaffolds was determined by changes in the scaffold's microstructure due to the dissolution/precipitation processes that take place after immersion in SBF. The characterization was performed by SEM and ICP-OES. Both samples are bioactive, because they generated a Hydroxyapatite (HA) precipitate, mineral

component of bone tissue, on its surface. However, SG scaffolds exhibited slower bioactivity (14 d) compared to BR (6 h), thus presenting different reaction kinetics.

RESUMEN

El aumento de la esperanza de vida en una población conlleva al envejecimiento de la misma, aumentando así la probabilidad de sufrir problemas relacionados con el tejido óseo. Es por tanto necesario el desarrollo de biomateriales destinados a la regeneración de tejido óseo.

En esta tesis se propone la obtención de materiales cerámicos, dentro del sistema $\text{Ca}_2\text{SiO}_4\text{-Ca}_3(\text{PO}_4)_2$, mediante la técnica de Réplica de Esponja Polimérica (REP) por inmersión de una esponja de poliuretano (PU) en una suspensión de Sol-gel (SG) y otra de Barbotina (BR), seguida de un tratamiento térmico para obtener cerámicas con una estructura 3D porosa. Posteriormente se procede a la caracterización físico-química, mineralógica, macro- y microestructural de los materiales previamente obtenidos, así como la evaluación de su bioactividad mediante ensayos, *in vitro*, en suero fisiológico artificial (SFA) con el objeto de estudiar su posible aplicación en la regeneración de tejido óseo.

La caracterización de los materiales obtenidos por ambos métodos se ha llevado a cabo por diferentes técnicas, tales como DRX, MEB, ATR-IRTF y Porosimetría de Hg. Los resultados indican que los andamios obtenidos por SG y BR poseen similitudes a nivel macroestructural. No obstante, presentan diferencias en cuanto a las fases presentes, microporosidad y microestructura.

Los andamios presentan una estructura de porosidad abierta (~95 %), cuyo tamaño de poro oscila entre 300-600 μm . Sin embargo, diferencias significativas se han encontrado en relación a la microporosidad, siendo del 12,83% y 48,9% en los andamios de BR y SG, respectivamente. En cuanto a la composición mineralógica, los andamios de BR son bifásicos debido a la presencia de las fases C_2S y Nurse's A, mientras que los andamios de SG son multifásicos, ya que presentan diversas fases minoritarias y C_2S y TCP como fases mayoritarias. Los resultados muestran una microestructura laminar alternando láminas de C_2S y Nurse's A para andamios de BR, mientras que los andamios de SG presentan una microestructura globular generada por una aglomeración de partículas que han perdido su identidad y han crecido de forma cilíndrica.

La evaluación de la bioactividad de los andamios se determinó mediante cambios producidos en la microestructura de los mismos debido a los procesos de

disolución/precipitación que tienen lugar tras inmersión en SFA. La caracterización se realizó mediante MEB y ICP-OES. Ambas muestras son bioactivas, ya que generaron un precipitado de Hidroxiapatito (HA), componente mineral del tejido óseo, en su superficie. Sin embargo, la cinética de reacción fue distinta, siendo más lenta para los andamios de SG (14 d) frente a los de BR (6 h).

1. INTRODUCCIÓN

El hecho de que la esperanza de vida de la población mundial haya aumentado, pone de manifiesto una evolución notoria en las terapias y los tratamientos sanitarios empleados. Esto conlleva una población mundial envejecida. Así el número de personas de más 60 años se ha duplicado en todo el mundo desde 1980 y se prevé alcanzar la cifra de 2000M en el 2050 [1]. Este rango de población se caracteriza por la descoordinación neuromuscular y la disminución de las funciones cognitivas. De este modo, el envejecimiento se asocia a patologías tales como fracturas, osteoartritis, osteoporosis y cáncer de hueso, entre otros [2].

De acuerdo con los datos ofrecidos por la OMS, 3,5M de personas padecen osteoporosis en España, y en Europa un total de 27,5M. En España, el número de fracturas causadas por caídas o fragilidad ósea asciende a 100.000/año, mientras que, en Europa, el número de fracturas de cadera producidas por fragilidad, en el 2010, fue de 610.000. Además, en nuestro país se contabilizan entre 63.000 y 65.000 fracturas de cadera/año en personas de avanzada edad [3]. Alejándonos del marco europeo, 31M de estadounidenses sufrieron osteoartritis en el 2012 y se estima que el número de pacientes con dicha patología ascienda a 67M en 2030 [4].

Todas estas complicaciones tienen un gran impacto a nivel clínico, social y sobretodo, económico. En 2010, los costes directos asociados a fracturas causadas por fragilidad ascendieron a 29.000M de euros en cinco países de la UE (España, Italia, Francia, Alemania y Gran Bretaña) y a 38.700M en toda la UE [3]. Por otra parte, en EE. UU se realiza aproximadamente, 1M de reemplazos de rodilla y de cadera al año, lo que supone un coste de 25.000M de dólares [5]. Además, se necesitan injertos óseos para más de 600.000 casos alcanzados en EE. UU causados por patologías en el tejido óseo cuya cifra en costos, asciende a 2500M de dólares [6].

A la vista de las estadísticas, surge la necesidad, a nivel mundial, de satisfacer dos grandes problemas: (1) tratamiento del deterioro de la salud de la población envejecida y (2) disminución de los costes sanitarios para poder tratar a un mayor número de pacientes [7].

Actualmente, la investigación básica está realizando esfuerzos titánicos para hallar la solución a las patologías que afectan al tejido óseo y abaratar sus costes. No obstante, los

hallazgos producidos recientemente se encuentran muy lejos de las aplicaciones clínicas. En nuestros días, dichas patologías se solucionan gracias a la cirugía ortopédica-restauradora cuyos tratamientos quirúrgicos, para fracturas o reemplazos, se basan en la utilización de implantes. Pero, tales implantes pueden ocasionar inconvenientes debido a micromovimientos del mismo y su posible aflojamiento aséptico, ocasionando inflamación, resorción ósea, osteolisis, desgaste y carga inadecuada [8].

Es por ello, que la cirugía ortopédica-restauradora combina tratamientos de activación de los mecanismos de regeneración de tejidos a nivel celular con la utilización de biomateriales con el fin de abordar la necesidad de regenerar tejidos, así como mejorar la biocompatibilidad de los distintos implantes. Por otra parte, estos biomateriales tienen una importancia significativa en el campo de la odontología, ya que no solo permiten devolver la funcionalidad de aquellas piezas dentales afectadas por patologías bucodentales como caries, sino que también permiten devolver la estética sustituyendo piezas dentales perdidas mediante el uso de implantes. Utilizando este tipo de biomateriales se pretende mejorar la calidad de vida de los pacientes y reducir los costes sanitarios.

1.1. Biomateriales y su clasificación.

Entendemos por biomaterial *“cualquier sustancia, que no sea un medicamento o una combinación de sustancias, naturales o sintéticas, que pueden ser utilizadas por un período de tiempo, independientemente o como parte de un sistema que trata, reemplaza o regenera cualquier tejido, órgano o función del cuerpo”*. Estos biomateriales destinados a la fabricación de implantes, deben poseer un conjunto de propiedades inamovibles cuando estén en contacto con el medio biológico (no tóxicos, resistentes a la corrosión, bioabsorbibles...), ya que los fluidos corporales proporcionan un ambiente altamente agresivo para los materiales debido a la presencia de enzimas, ácidos orgánicos y otro tipo de factores externos [9].

Actualmente, los biomateriales representan un campo relevante para la investigación y la innovación debido a su gran versatilidad y a sus infinitas aplicaciones en los campos médico-sanitarios, hecho por el cual poseen un gran interés económico. Dichos materiales se pueden clasificar dependiendo de su función, interacción con el tejido, naturaleza y su generación.

Atendiendo a su función.

Dependiendo de la función que desempeñen dentro o fuera del organismo pueden ser materiales destinados al soporte con una finalidad ortopédica (caderas, vertebras, rodillas...), pueden estar destinados a reemplazar zonas del sistema cardiovascular (válvulas cardíacas), pueden ir dirigidos a la ingeniería maxilofacial como implantes dentales o rellenos maxilofaciales, pueden ser diseñados para la cura de heridas producidas en tejidos blandos, incluso formar parte de dispositivos de diagnóstico y de instrumentos quirúrgicos. Por otra parte, también pueden actuar como transportadores y/o dosificadores de fármacos, liberándolos en un radio controlado [9].

Atendiendo a la interacción Biomaterial-Tejido.

Dependiendo de cómo interactúen con el tejido, se pueden subdividir en bioinertes, bioactivos y bioreabsorbibles [9].

Los **biomateriales inertes** son aquellos que mantienen una interacción mínima con el tejido en el que han sido implantados, permaneciendo, de esta forma, aislados del entorno mediante la formación de tejido fibroso alrededor del mismo. Los **materiales bioactivos** son aquellos que inducen una respuesta biológica específica y establecen conexiones con el tejido óseo huésped [10]. Finalmente, los **materiales bioreabsorbibles** son materiales que son degradados y/o asimilados por el cuerpo humano de una forma lenta y gradual [9].

Atendiendo a su naturaleza.

Pueden ser de origen natural o sintético. Éstos últimos, a su vez pueden subdividirse en polímeros, cerámicos, metálicos o composites [9].

Atendiendo a su generación.

Dependiendo del momento en el que se desarrollaron los materiales y las propiedades de los mismos se pueden subdividir en primera, segunda o tercera generación. El objetivo principal de un material de **primera generación** es *"lograr una combinación adecuada de propiedades físicas para que coincidan con las del tejido reemplazado sin respuesta tóxica en el anfitrión"* [11]. Son materiales que se han desarrollado para utilizarse en el interior del cuerpo humano a modo de prótesis. Los materiales de **segunda generación** comparten las mismas características que los de la primera, pero además son bioactivos

o reabsorbibles, mientras que los materiales de **tercera generación** poseen ambas propiedades y estimulan la regeneración de tejido óseo, la proliferación y diferenciación celular [12,7].

Sin embargo, a pesar de la gran versatilidad que poseen los biomateriales, hemos de ser cautos, ya que el tejido humano es extremadamente sensible a sustancias extrañas y la aplicación incorrecta de este tipo de biomateriales podría desencadenar respuestas de rechazo en los tejidos circundantes [9]. Los biomateriales utilizados en el cuerpo humano pueden desencadenar diferentes respuestas en los tejidos [13].

- A) Material tóxico → Muerte celular. (por lo que no se consideraría biomaterial).
- B) Material no tóxico y reabsorbible → El tejido circundante lo sustituye.
- C) Material no tóxico y bioinerte → Formación de cápsula fibrosa alrededor del material
- D) Material no tóxico y bioactivo → Unión química interfacial tejido-biomaterial.

1.2. Ingeniería de Tejidos y Biocerámicas.

La medicina regenerativa es una disciplina cuyo objetivo consiste en reparar o regenerar tejidos heridos o perdidos, así como recuperar funciones de órganos.

Se pueden distinguir dos grandes campos en la medicina regenerativa: (1) investigación regenerativa y (2) terapia regenerativa. El primer campo posee dos objetivos claramente diferenciados: (i) investigar biológicamente las células para clarificar su desempeño en la regeneración tisular y (ii) descubrir nuevos fármacos para evaluar su toxicidad con células vivas. Por otra parte, el objetivo de la terapia regenerativa es tratar patologías mediante la inducción *in vivo* de actividad celular destinada a la regeneración tisular [14].

Para satisfacer los objetivos propuestos por la medicina regenerativa nació una disciplina denominada ingeniería de tejidos, la cual se aplicaba hasta mediados de los 80 en casos de manipulación quirúrgica de tejidos u órganos [15].

En 1993, Langer y Vacanti [11] definieron esta disciplina de la siguiente forma: “*La ingeniería de tejidos es un campo interdisciplinario que aplica los principios de la ingeniería. y ciencias de la vida hacia el desarrollo de sustitutos biológicos que*

restauran, mantienen o mejoran la función del tejido". Esta disciplina crea dispositivos con un alto potencial, destinados a la integración y regeneración de un tejido tras su implantación [15].

Tradicionalmente las patologías óseas se trataban mediante la utilización de implantes, ya fuesen autólogos (el tejido/células implantadas provienen del mismo paciente), alogénicos (el tejido/células implantadas provienen otro ser humano) o xenogénicos (el tejido/células implantadas provienen de una especie diferente). No obstante, la utilización de implantes, como *gold estándar*, tiene inconvenientes. En el caso de los autólogos, el principal inconveniente es la disponibilidad de tejido óseo, mientras que en el caso de los alogénicos y xenogénicos, es la presencia de respuesta inmunitaria en el organismo [8].

En nuestros días, la ingeniería de tejidos busca la creación de biomateriales cuyo objetivo principal sea la sustitución específica del tejido biológico dañado o la reparación del mismo, evitando lesiones o complicaciones que van ligadas a los métodos tradicionales.

En las últimas décadas, la ingeniería de tejidos ha estado investigando en el campo de las biocerámicas cuyo principal campo de aplicación es la ingeniería de tejido óseo, ya sea en el sistema esquelético, odontología o cirugía maxilofacial [15,16,17]. Estas biocerámicas se definen, teniendo en cuenta la norma ISO/TR 109939:1994 (E), como *"Material cerámico diseñado para lograr un comportamiento fisiológico específico al ser usado en la reconstrucción de prótesis u órganos artificiales internos"*. La composición química y la topografía de superficie de una biocerámica son de vital importancia, ya que estos parámetros van a influir en la adsorción de proteínas, interacción celular y respuesta del tejido huésped [18]. Es por ello que sus principales representantes son los materiales de Si-P-Ca, ya que presentan una analogía con la fase mineral del hueso, en términos estructurales y de composición química [19]. Además, presentan propiedades conductivas y son capaces de proporcionar una interfaz biocompatible entre la superficie del material y el propio tejido óseo sin formar tejido cicatricial [20,21]. Estas biocerámicas son porosas, bioactivas y reabsorbibles, reaccionan con el medio y se degradan gradualmente durante un periodo de tiempo concreto mientras son reemplazadas por el tejido huésped, por lo tanto, desaparecerán una vez hayan cumplido su papel. [22,23].

Por otra parte, encontramos biocerámicas generadas a partir de HA sintético ($\text{Ca}_{10}(\text{PO}_4)_6(\text{OH})_2$) que, desde un punto de vista cristalográfico, es la fase de fosfato de calcio que más se asemeja a la apatita del hueso natural. Sin embargo, las propiedades químicas del HA sintético difieren del HA del hueso. El HA sintético es más estable y, por tanto, la tasa de reabsorción es más lenta que la de regeneración ósea. A modo de solución, se pueden generar biocerámicas derivadas del HA, mezclando fosfatos cálcicos con una tasa de reabsorción más rápida, como el β -TCP. De esta forma se han creado distintas formulaciones bifásicas HA/ β -TCP [24].

Así, el HA se utiliza como material bioactivo destacado en atención médica debido a su biocompatibilidad, no toxicidad y propiedades osteoconductoras. Además, puede favorecer la adhesión y proliferación de osteoblastos y osteoclastos, así como inducir diferenciación osteogénica de células madre. No obstante, estos materiales poseen baja resistencia a la tracción y a la fractura, ya que son rígidos, pero quebradizos. Estas biocerámicas no se utilizan principalmente para la fabricación de prótesis completas que soporten grandes cargas. Su principal uso es en forma de polvo o partículas de diverso tamaño, aunque también se usa en la obtención de andamios porosos destinados a injertos o en rellenos óseos, así como en recubrimientos para biofuncionalizar prótesis metálicas [25].

No obstante, para que las biocerámicas sean consideradas como aspirantes óptimos en el campo de la ingeniería de tejido óseo, no basta con una composición química y una topografía superficial adecuada, sino que han de poseer una estructura tridimensional con una red interconectada de poros abiertos cuyo objetivo es simular la estructura y propiedades mecánicas del hueso trabecular. Esta estructura porosa desempeña un papel fundamental en la regeneración ósea, ya que modulará el proceso de osteogénesis mediante el control de la migración y proliferación celular a través del material, angiogénesis, suministro de nutrientes, liberación de desechos, y circulación de productos celulares [15,26,27,28,29].

Por otro lado, la presencia de silicio en la composición de las biocerámicas desempeña un papel fundamental en la regeneración ósea. El silicio está involucrado en el proceso de mineralización, formación y remodelación ósea. También mejora la bioactividad, la proliferación de osteoblastos y la diferenciación de CMM y protoblastos a linajes osteogénicos [30,31,32].

Las propiedades que han de poseer este tipo de biocerámicas, para cumplir el propósito principal de la ingeniería de tejidos, son las siguientes [15]:

- Propiedades mecánicas adecuadas. Debe soportar el manejo de la cirugía y las cargas en el lugar de implantación, proporcionando un soporte temporal en el tejido implantado.
- Resistencia a la corrosión en ambientes acuosos. El biomaterial estará implantado en el interior del organismo exponiéndose a fluidos corporales altamente corrosivos y degradativos.
- Biocompatibilidad. Creación de una interfaz entre la superficie del biomaterial/tejido implantado sin procesos cicatriciales, ni respuesta inmunitaria, a la vez que mantiene la actividad celular normal incluyendo señalización molecular sin efectos locales tóxicos y sistémicos para el tejido huésped
- Biodegradabilidad. Reabsorción del material, de forma gradual y controlada, a medida que va siendo sustituido por tejido nuevo.
- Bioactividad. Capacidad de crear una capa de HA en la superficie del material y en el interior cuando éste está en contacto con fluidos corporales.
- Osteoconductividad. Presencia de una red porosa interconectada que promueva la penetración y proliferación celular, y que permita la vascularización del sistema, favoreciendo el transporte de nutrientes y la eliminación de residuos celulares.
- Osteoinductividad. Capacidad del material para promover diferenciación celular hacia linajes osteogénicos.

1.3. Diagrama de fases aplicados al diseño de biomateriales.

El diseño de una biocerámica requiere el conocimiento de la composición, fases y microestructura de la misma. Esta información se puede obtener a partir de los diagramas de equilibrio de fases que son utilizados para predecir y entender el comportamiento de un material con respecto a las variables de estado (temperatura, presión y composición química), y son representaciones gráficas de las condiciones termodinámicas de equilibrio de un sistema. Aplicando estos diagramas podemos diseñar una amplia variedad de materiales siguiendo su tendencia termodinámica (fases estables y condiciones de equilibrio). Se entiende como estado de equilibrio termodinámico de un

sistema aquel en el cual sus propiedades no cambian con el tiempo, a menos que se ejerza una variación de temperatura, presión o composición. Los diagramas de fase más comunes representan temperatura frente a composición química, dado que la mayoría de las reacciones tienen lugar a presión atmosférica.

El fundamento teórico en el que se basan los diagramas de fases es la ley de Willard Gibbs, conocida como la regla de las fases, que para sistemas no condensados es: $F+L=C+2$. Donde L= grados de libertad; F= número de fases presentes en el equilibrio; C= Número de componentes del sistema; 2= Variables de estado (Temperatura, presión y composición). Si se tratase de un sistema condensado, la fórmula se reescribiría de la siguiente forma: $F+L=C+1$.

Esta ley nos indica la relación existente entre el número de fases y el número de variables de estado independientes. La aplicación de dicha ley mostrará como varía el equilibrio cuando ocurren variaciones en dichas constantes. De esta manera, representando esquemáticamente el equilibrio de fases en función de las variables de estado, se construyen los diagramas de equilibrio de fases. La mayoría de los diagramas se clasifican dependiendo de las reacciones invariantes que ocurran en el mismo. Si la reacción tiene lugar en presencia de fase líquida, podemos encontrar, entre otras, reacciones eutécticas, monotécticas y peritécticas. No obstante, si se trata de una reacción en estado sólido donde hay ausencia de fase líquida, podemos encontrar, entre otras, reacciones eutectoides, peritectoides, etc...

1.3.1. Biomateriales en el sistema $\text{Ca}_2\text{SiO}_4\text{-Ca}_3(\text{PO}_4)_2$

El sistema binario Silicato dicálcico (Ca_2SiO_4 , C_2S) – Fosfato tricálcico ($\text{Ca}_3(\text{PO}_4)_2$, TCP) fue estudiado por primera vez por Nurse y col. en 1959 [33] utilizando microscopía de alta temperatura y rayos X. En él se identificaron dos compuestos intermedios formados por reacción en estado sólido a bajas temperaturas: la silicocarnotita, estable por debajo de 1450 °C, y una nueva fase denominada “Nurse’s A”, estable por debajo de 1125 °C que posee una composición estequiométrica $7\text{CaO}\cdot\text{P}_2\text{O}_5\cdot 2\text{SiO}_2$ que no debe confundirse con el mineral de la misma composición identificado como Nagelshdmedita [33]. Para cualquier proporción de $\text{C}_2\text{S}/\text{TCP}$ se encontró una solución sólida de alta temperatura formada por $\alpha\text{-C}_2\text{S}$ y $\alpha'\text{-TCP}$ denominada “R”, la cual es metaestable a temperatura ambiente. Posteriormente dicho diagrama fue modificado por Fix y col. [34],

incluyendo cambios importantes referentes a la extensión de los campos de las fases sólidas:

- La solución sólida correspondiente a la silicocarnotita tiene un campo de estabilidad menor que el que describe Nurse y col. Además, el punto eutectoide Silicocarnotita-TCP también se modifica.
- La fase Nurse's A puede transformarse a fase "R" sobre los 1350 °C.
- Fue posible obtener fase "R" metaestable a temperatura ambiente no solo mediante enfriamiento rápido (*quenching*), sino también por enfriamiento lento, a bajas concentraciones de TCP.

Todos estos cambios modifican notablemente el diagrama inicialmente propuesto por Nurse y col. [32]. Por otra parte, el diagrama de Fix y col. ha sido modificado recientemente por Rubio y col. [35], por Martínez y col. [36], y por P. Ros y col. [37] en los cuales se han realizado revisiones parciales de dicho sistema que han conducido a la modificación de los tres puntos invariantes eutectoides dentro de los subsistemas C₂S-Fase Nurse's A, Fase Nurse's A-Silicocarnotita y Silicocarnotita-TCP.

1.3.2. Silicato dicálcico: C₂S (Ca₂SiO₄)

El silicato dicálcico existe en varias formas polimórficas, de baja a alta temperatura, que son α , α' , β y γ . De los polimorfismos mencionados, solo la forma γ es metaestable a temperatura ambiente sin la necesidad de ningún estabilizante. Por otra parte, la forma β se encuentra comúnmente en el cemento Portland, constituyendo además, una fase importante para prótesis cementadas utilizadas en odontología [38]. El C₂S es un importante constituyente de materiales refractarios y recubrimientos resistentes al calor, no obstante, recientes estudios, como el de Gou y col. [39] han demostrado el potencial del C₂S como biomaterial debido a su buena bioactividad, biocompatibilidad y sus propiedades mecánicas [38].

1.3.3. Fosfato tricálcico: TCP (Ca₃(PO₄)₂)

El TCP presenta tres polimorfismos, de baja a alta temperatura, que son β , α , y α' , de los cuales, solo dos (α -TCP, β -TCP), son utilizados para la fabricación de biomateriales, ya que α' -TCP no es estable a temperatura ambiente. Las aplicaciones que presentan los materiales basados en TCP están prácticamente limitadas a cementos de α -TCP, los cuales son usados en cirugía odontológica, craneofacial y maxilofacial, así como en

procedimientos de vertebroplastia y cifoplastia. También pueden desempeñar la función de transportadores de fármacos [40].

Por otra parte, en 1986, se acuñó el término fosfato de calcio bifásico (FCB) para describir una biocerámica que consistía en una mezcla de HA y β -TCP. Los FCB pertenecen a una familia de cerámicas bifásicas que combinan la baja solubilidad y osteoconductividad de HA con la osteoinductividad de una fase más soluble como TCP. Incluyen diferentes proporciones de HA/ β -TCP, HA/ α -TCP y, más recientemente, incluso β -TCP/ α -TCP

Estos FCB comerciales están disponibles como bloques, partículas (gránulos) y formas personalizadas, como cuñas para osteotomía de apertura tibial, conos para columna y rodilla e insertos para fusión de la caja vertebral [41].

2. OBJETIVOS

Los biomateriales cerámicos 3D con porosidad abierta son candidatos para ser utilizados en ingeniería de tejidos óseos, por lo que mediante la información proporcionada por el diagrama de equilibrio de fases $2\text{CaO}\cdot\text{SiO}_2\text{-}3\text{CaO}\cdot\text{P}_2\text{O}_5$ se pretende, como **objetivo principal** de esta tesis, diseñar y sintetizar un material cerámico de composición eutéctico (31% en peso TCP ($3\text{CaO}\cdot\text{P}_2\text{O}_5$) – 69% en peso C_2S ($2\text{CaO}\cdot\text{SiO}_2$), que posteriormente se caracteriza física, química, mineralógicamente y se evalúa su bioactividad y biocompatibilidad, *in vitro*, en forma de andamios, con una elevada porosidad interconectada que favorezca sus capacidades osteogénicas.

Para desarrollar el objetivo principal de la tesis se plantean varios objetivos parciales:

- I. Métodos de conformado para la síntesis de los andamios. Se ha utilizado el método REP, tanto en BR como en SG.
- II. Optimización de la síntesis.
- III. Caracterización físico-química, mineralógica, micro y macroestructural de los andamios.
- IV. Estudios de bioactividad *in vitro*, en SFA de los andamios y análisis de los procesos de disolución/precipitación en la interfaz de reacción en función del tiempo de inmersión en SFA.

3. MATERIALES Y MÉTODOS

3.1. Andamios 3D porosos en Barbotina.

El polvo cerámico destinado a la producción de andamios porosos fue sintetizado mediante una reacción en estado sólido, en la cual se mezclaron, en cantidades estequiométricas, hidrogeno fosfato cálcico anhídrico ($\text{CaHPO}_4 > 98.0 \%$, Acros), carbonato cálcico ($\text{CaCO}_3 > 99.0 \%$, Acros) y dióxido de silicio ($\text{SiO}_2 > 99.7 \%$, Stream Chemicals) para obtener la composición eutectoide final 31% en peso TCP ($3\text{CaO}\cdot\text{P}_2\text{O}_5$) – 69% en peso C_2S ($2\text{CaO}\cdot\text{SiO}_2$), que tras la síntesis especificada en el apartado “*Materials and processing methods*”, del primer artículo (pág. 35) y en el apartado “*Materials and Methods*”, del segundo artículo (pág. 71-74), sirvieron como material de partida para elaborar una barbotina. Se preparó una suspensión al 60% en sólidos donde se impregnaron las esponjas de PU, que tras los tratamientos térmicos adecuados (véase el apartado “*Creation of ceramic 3D porous scaffold*”, del primer artículo (pág.35-36) y el apartado “*Materials and Methods*”, del segundo artículo (pág. 71-74)) dió lugar a la obtención de unas estructuras 3D con porosidad abierta.

Seguidamente, las estructuras cerámicas 3D se caracterizaron mediante el empleo de las técnicas instrumentales citadas en el apartado “*Characterisation of ceramic 3D porous scaffolds*”, del primer artículo (pág. 36-37) y en el apartado “*Materials and Methods*”, del segundo artículo (pág. 71-74).

3.2. Andamios 3D porosos en Sol-Gel.

Para elaborar la solución de Sol-Gel, en la cual se impregnaron las esponjas de PU, se partió de una reacción en estado líquido mezclando las cantidades estequiométricas de tetra-etil-ortofosfato (TEP, Aldrich-98%, St. Louis, MO, USA), tetra-etil-ortosilicato (TEOS, Aldrich-98%, St. Louis, MO, USA), carbonato cálcico (CaCO_3 , Sigma, $> 99\%$, St. Louis, MO, USA), agua, etanol y ácido clorhídrico, para obtener la misma composición eutectoide citada anteriormente. Las condiciones y parámetros de procesamiento son los citados en el apartado “*Materials and Methods*”, del segundo artículo (pág. 71)

Una vez obtenidos los andamios cerámicos 3D porosos, éstos fueron completamente caracterizados mediante las técnicas instrumentales mencionadas en el apartado “*Materials and Methods*”, del segundo artículo (pág. 73-74).

3.3. Bioactividad

El ensayo se llevó a cabo siguiendo el protocolo propuesto por Kokubo y col. en 2006 [42] e incorporado en la norma ISO/FDIS 2331:2014, mediante la inmersión de la esponja en SFA a diferentes periodos de tiempo y analizando tras los mismos, la morfología de la superficie y las concentraciones iónicas del SFA. Las condiciones y tiempos de ensayo, así como las técnicas de análisis de los resultados, se especifican en el apartado “*Bioactiviy analysis*”, del primer artículo (pág. 37) y en el apartado.” *Materials and Methods*”, del segundo artículo (pág. 74). El tiempo de inmersión en SFA en el caso de los andamios de Sol-gel fue de 3d a 14d, mientras que en el caso de la barbotina de 6h a 21d.

4. RESULTADOS.

En la presente tesis doctoral se han desarrollado biomateriales cerámicos bifásicos y multifásicos mediante el método REP por inmersión de una esponja de PU en una suspensión de BR y SG dentro del sistema silicato dicálcico– fosfato tricálcico. Las variables de procesado se han estudiado y optimizado para ambos métodos, seguido de la caracterización de los andamios porosos. Finalmente, la posible aplicación de los mismos como andamios en ingeniería de tejido óseo se ha determinado mediante ensayos de bioactividad, *in vitro*, en SFA.

4.1. Andamios 3D porosos en Barbotina.

Caracterización

En el análisis mediante DRX de la cerámica utilizada para preparar la barbotina se observaron dos fases cristalinas claramente diferenciadas: α' -C₂S y Nurse's A (Fig. 1. Artículo 1). Dichas fases no cambiaron después del procesado de los andamios. El tiempo de molienda óptimo establecido para el material fue de 2h, ya que, a este tiempo, la distribución de tamaño de partícula fue la más estrecha, presentando un tamaño de partícula promedio de 13,76 μ m en el 50% de la muestra (Fig.2. Artículo 2).

Los andamios porosos presentaron la misma estructura macroscópica que las plantillas de PU, a pesar del 37,3% de contracción que sufrieron tras el tratamiento térmico (Fig. 3. Artículo 1). Tras ser analizados por microscopía electrónica de barrido (MEB) se observó la presencia de una estructura 3D porosa con poros interconectados cuyo tamaño oscilaba entre los 300-600 μ m. Además, también se observó una topografía típica del punto eutectoide, constituida por láminas alternadas de Nurse's A y α' -C₂S. (Fig. 4. Artículo 1). Los andamios exhibieron un 95 % de macroporosidad y un 12,8% de microporosidad (8,76% de microporosidad interparticular y 4,07% de microporosidad intraparticular (Fig. 6. Artículo 1). Por último, la espectroscopía de infrarrojo IRTF mostró que los enlaces químicos presentes en los andamios correspondieron a grupos fosfatos (PO_4^{3-} /515, 538, 584 cm^{-1} /1000-1300 cm^{-1}) y a la red de silicatos (Si-O-Si/873 cm^{-1} /1080-1100 cm^{-1}), los cuales presentaron distintos modos vibracionales como: estiramiento simétrico/antisimétrico y flexión (Fig. 5. Artículo 1).

Bioactividad.

Los ensayos de bioactividad *in vitro* mostraron un cambio significativo en la morfología superficial de los andamios debido a la rápida precipitación de una capa de HA en la superficie del material, en las primeras etapas del ensayo (6h) (Fig. 7. Artículo 1). Tras ensayos de IRTF, dicha capa fue identificada como carbo-hidroxiapatito (CHA), ya que su patrón de infrarrojo presentaba grupos químicos OH⁻ y C-O a 3000-3600cm⁻¹ /1600cm⁻¹ y a 1450-1490cm⁻¹, respectivamente (Fig. 8. Artículo 1).

Finalmente, los procesos de precipitación/disolución estudiados mediante espectrometría de emisión óptica de plasma acoplado inductivamente (ICP-OES) (Fig. 9. Artículo 1) nos ayudaron a comprender el comportamiento de los materiales cerámicos 3D tras la inmersión en SFA. A etapas tempranas de dicho ensayo (3h-1d) se produjeron dos procesos de manera simultánea: (I) disolución del andamio cerámico poroso, y (II) precipitación de CHA en la superficie del material. A etapas tardías del ensayo (7d-21d) se produjo una precipitación masiva de CHA en la superficie del material.

4.2. Andamios 3D porosos en Sol-Gel

Caracterización

Los andamios 3D porosos obtenidos por inmersión de una esponja de PU en una suspensión de Sol-gel presentaron 5 fases tras ser analizados mediante DRX: Tridimita, Cristobalita, Fosfato tricálcico, Pirofosfato y α' -Silicato dicálcico (Fig. 1. Artículo 2). Éstos presentaron una estructura porosa con poros interconectados cuyo tamaño oscilaba entre 300-500 μ m. La microestructura superficial reveló una aglomeración de partículas que experimentaron un crecimiento considerable de grano hasta aproximarse a partículas cilíndricas (Fig. 3. Artículo 2). Dichos andamios, tras ser analizados mediante porosimetría de mercurio, presentaron un 94,8% de macroporosidad y un 48,9% de microporosidad (39,66% de microporosidad interparticular y 9,24% de microporosidad intraparticular) (Fig. 6. Artículo 2).

Finalmente, los enlaces químicos presentes en los andamios 3D correspondieron a grupos fosfatos (PO₄³⁻/560-585cm⁻¹/900-1100cm⁻¹) y a la red de silicatos (Si-O-Si/1000-1300cm⁻¹, Si-O-2NBO/848cm⁻¹ y Si-O-NBO/840-975cm⁻¹), los cuales presentaron

distintos modos vibracionales como: estiramiento simétrico/antisimétrico y flexión (Fig. 2. Artículo 2)

Bioactividad

Los ensayos de bioactividad *in vitro* no mostraron ningún cambio en la superficie de los andamios en etapas tempranas. Sin embargo, mostraron una precipitación tardía de la capa de HA en la superficie del material (14d). Dicho precipitado estaba formado por partículas de forma esférica con un diámetro promedio de 30 μ m, que al unirse entre sí formaron una capa continua y compacta. Dicha capa, debido al secado de la muestra antes del estudio por MEB, mostró un craqueo, indicando que se había depositado una capa relativamente gruesa de HA. (Fig. 7. Artículo 2).

Atendiendo a los procesos de disolución/precipitación, se pudo comprender cómo reaccionan los andamios porosos cuando están en contacto con el suero. En este caso la concentración en suero de los iones de Si, Ca y P aumentó hasta los 3d, implicando la disolución del andamio, mientras que de 7d-14d hubo un descenso de la concentración de los iones Ca y P, indicando la formación y precipitación de la capa de HA en la superficie del material (Fig. 9. Artículo 2)

5. DISCUSIÓN.

La ingeniería de tejidos está en continuo desarrollo y la creación de sustitutos óseos biosintéticos ha experimentado mejoras notables, llegando al punto de eliminar el uso de injertos autólogos óseos [43]. Mejoras en este tipo de materiales son necesarias para una mejor interacción entre el material y el tejido huésped [44]. Como consecuencia, se generan nuevas estructuras capaces de reparar, restaurar y regenerar tejido óseo dañado. Es por ello que el material ideal para la regeneración de tejido óseo debe poseer una estructura y propiedades mecánicas similares a las del hueso. Además, ha de ser al mismo tiempo bioactivo, biocompatible, osteoinductivo, osteoconductor, osteogénico y biodegradable en productos no tóxicos para las células, ya que actúa como un soporte temporal. Finalmente debe poseer una estructura 3D de poros abiertos, porque ésta modulará el proceso de formación de tejido óseo mediante el control del suministro de nutrientes, la circulación de productos celulares de desecho, angiogénesis y contacto celular desde el interior del mismo [45,46,47,27,26,27].

Después de considerar todos los aspectos anteriormente mencionados, en esta tesis se ha llevado a cabo el procesamiento y la caracterización de nuevos andamios cerámicos porosos bioactivos, producidos por REP en una suspensión de SG y BR de una composición eutéctica del 31% en peso TCP-69% en peso C₂S dentro del sistema C₂S-TCP [35].

La caracterización mineralógica de los andamios producidos por BR muestra un material bifásico compuesto por las fases α' -C₂S y Nurse's A (Fig. 1. Artículo 1), de acuerdo a la línea de Alkemade Ca₂SO₄-Ca₃P₂O₈ contenida en el sistema SiO₂-CaO-P₂O₅ [48]. Sin embargo, en el caso del SG, los precursores (TEOS/TEP), total o parcialmente hidrolizados, se unen entre sí por una reacción de condensación y polimerización [29]. A partir del TEOS se generan las uniones Si-O-Si, y a partir del TEP se generan las P-O-P. Tras la sinterización de los andamios, las uniones Si-O-Si inducen la formación de las fases polimórficas SiO₂ y Ca₂SiO₄, mientras que las uniones P-O-P favorecen la formación de Ca₃P₂O₈ y Ca₂P₂O₇. Como consecuencia se produce una desviación en la línea de Alkemade Ca₂SO₄-Ca₃P₂O₈, implicando la presencia de múltiples fases en los andamios generados por SG (Fig. 1. Artículo 2).

Independientemente del método de procesado, se obtuvo una alta porosidad a nivel macroscópico (~95%). Esta red tridimensional podría mejorar la distribución celular en

el andamio y la difusión a través del mismo, de nutrientes y metabolitos celulares. Los andamios mantuvieron la misma estructura tridimensional que las esponjas de PU. Además, el tamaño de poro de la red 3D es muy similar en ambos andamios (300-500 μm para SG y 300-600 μm para BR). Esta pequeña diferencia se debe a la diferente cantidad de recubrimientos que fue necesaria en cada caso para obtener una adecuada manipulabilidad. En el caso del SG se realizaron 25 recubrimientos mientras que solamente 3 fueron necesarios para los andamios de BR. La microestructura de ambos andamios mostró diferencias significativas. Los andamios de BR presentaron una topografía específica mostrando rosetas que se asemejaron a la microestructura laminar típica de la composición eutectoide observada por Rubio y col., que trabajaron con el material denso en 2011 [35]. Mientras que los andamios de SG mostraron una aglomeración de partículas cilíndricas que perdieron su identidad y experimentaron un crecimiento considerable de grano (Fig. 4. Artículo 1 y Fig. 3 y 4. Artículo 2).

Analizando la microporosidad de los andamios obtenidos por ambos métodos, mediante porosimetría de Hg, los resultados fueron el 48,9% y el 12,83% de microporosidad total para las muestras de SG y de BR, respectivamente. Considerando microporosidad intraparticular ($1\mu\text{m} < \text{Ø Poro} < 300\mu\text{m}$) e interparticular ($\text{Ø Poro} < 1\mu\text{m}$), el 9,24% representó la microporosidad intraparticular de los andamios de SG y el 39,66% representó la interparticular. Por otra parte, en el caso de los andamios de BR, el 4,07% representó la microporosidad intraparticular, mientras que la interparticular quedó representada con un 8,76% (Fig. 6. Artículo 1,2). El hecho de que hayamos sintetizado andamios con distintos niveles de porosidad alcanzando la escala nanométrica, pone de manifiesto una estructura jerarquizada, la cual va a proporcionar múltiples ventajas correspondientes al proceso de bioactividad y regeneración de tejido óseo.

En la bibliografía se han encontrado discrepancias correspondientes al tamaño de poro ideal de un biomaterial. Está establecido por algunos autores que poros inferiores a 10 μm proporcionan una mayor área superficial repercutiendo en un mayor contacto entre la superficie y el hueso natural. Como consecuencia, aumenta el intercambio iónico en la interfase mejorando la bioactividad, la adsorción de proteínas y la nueva formación de tejido óseo [49,50,51].

Ascendiendo en la jerarquía del tamaño de poro, como regla general se puede decir que aquellos que rondan los 100-150 μm mejoran la adhesión celular de los osteoblastos

y facilitan su proliferación y migración a través del material [52,53]. Finalmente, aquellos que superan los 300 μ m favorecen la migración celular y la formación de una red de vasos sanguíneos a través del material cuyo principal propósito es el suministro nutricional a las células, así como la retirada de sus productos de desecho, los cuales son tóxicos para las propias células y las adyacentes [54,27,45,46]. A parte de la porosidad, las micro-macroestructuras mencionadas anteriormente también favorecen la adhesión celular, y su expansión, mejorando, así, las capacidades bioactivas y regenerativas de los andamios [28,48].

La caracterización de las uniones químicas presentes en los distintos andamios mediante el uso de la IRTF no mostró grandes diferencias entre los mismos. Los espectros obtenidos fueron caracterizados utilizando como referencia las unidades tetraédricas SiO_4^{4-} y PO_4^{3-} . Los resultados mostraron uniones características de silicatos cálcicos y fosfatos cálcicos. En ambas muestras se identificaron bandas relacionadas con grupos fosfato a bajas longitudes de onda (500-600 cm^{-1} /800-1100 cm^{-1}) y bandas relacionadas con la red de Si-O-Si a 800-1100 cm^{-1} . Pero dadas las similitudes de las unidades tetraédricas ($\text{SiO}_4^{4-}/\text{PO}_4^{3-}$) y debido a que las fases cristalinas inorgánicas comparten varios grupos vibracionales, se observó un solapamiento de dichas bandas (Fig. 5. Artículo 1 y Fig. 2. Artículo 2).

El estudio de bioactividad permite determinar la capacidad del material de inducir la formación de una capa de precipitado de HA en la superficie del mismo mediante la inmersión en SFA.

El estudio *in vitro*, sumergiendo andamios en SFA durante varios periodos de tiempo para evaluar la bioactividad de los materiales, mostró que ambos andamios son bioactivos, no obstante, presentaron distinta cinética de reacción. Los andamios de BR presentaron una bioactividad temprana (a las 6h de ensayo), mientras que los andamios de SG presentaron una bioactividad tardía (a los 14d de ensayo) (Fig. 7. Artículo 1 y Fig. 7 y 8. Artículo 2). Esta diferencia se debe a las fases cristalinas presentes en los andamios y a la microestructura superficial de los mismos. Por un lado, la caracterización mineralógica de los andamios de SG mostró que eran multifásicos, siendo una de las fases presentes el pirofosfato. Una baja concentración de pirofosfato inhibe o ralentiza, no solo el crecimiento, si no la precipitación de cristales de HA en la superficie de los materiales

tanto *in vitro* como *in vivo* [55,56,57]. Por otro lado, atendiendo a la microestructura superficial, las muestras de BR presentaron una microestructura laminar, y es en estas láminas donde se produce el mayor intercambio iónico entre el SFA y la muestra, acelerando, de esta manera, el mecanismo que produce la precipitación de HA.

Otros autores como Padilla y col. [58], Karamian y col. [59] y Lenka Novotna y col. [60], sintetizaron materiales bifásicos con una estructura granular, muy similar a la generada por los andamios de SG. Dichos autores evaluaron la bioactividad, utilizando la misma metodología citada anteriormente y los resultados obtenidos fueron muy similares a los obtenidos en los andamios de SG. En las muestras de SG la capa de HA se presentó a los 14d, mientras que en el caso de los tres autores mencionados anteriormente se visualizó a los 7d, 28d y 21d, respectivamente. Como se puede observar, contrastando la literatura con los resultados de esta Tesis Doctoral, los andamios que poseen una microestructura granular y pirofosfato presentan una cinética de reacción tardía frente a los materiales que exhiben una microestructura laminar y ausencia de pirofosfato. En la bioactividad de un biomaterial influye tanto su composición química como su microestructura superficial.

A la luz de estos resultados, el mecanismo de bioactividad se puede describir como procesos de disolución/precipitación. Para ello se ha determinado los cambios en la concentración de los iones Si, P y Ca en el SFA, tras el ensayo de bioactividad, mediante la técnica ICP-OES (Fig. 9. Artículo 1 y Fig. 9 Artículo 2).

Los resultados obtenidos en las muestras de BR reflejan que en la primera parte del ensayo, se está disolviendo una de las fases presentes en el material debido al incremento de la concentración de Si en el SFA. Además, se observó una pequeña reducción en la concentración de iones Ca en el SFA, que se corresponde con una ligera precipitación de HA. La fase que se está disolviendo debería ser la de C_2S , ya que solo las concentraciones de los iones Ca y Si aumentan en el SFA. Si se tratase de la disolución de la fase de TCP, aumentaría también la concentración de los iones P en el SFA. En la segunda parte del ensayo ocurren dos procesos de manera simultánea. La fase Nurse's A empieza a disolverse al mismo tiempo que ocurre la precipitación de HA. Esto queda reflejado por el incremento de la concentración de los iones Ca y por el descenso en la concentración de iones P, respectivamente. Destacar que la cantidad de iones Ca y P que se necesitan para precipitar la nueva capa de HA es mayor que la cantidad de iones que liberan los

andamios al SFA. Finalmente, una gran cantidad de HA se deposita en la superficie del material, siendo mecánicamente inestable, Como consecuencia, ésta se desprende de la superficie y cae al suero aumentando las concentraciones de iones Ca y P (Fig. 8 y 9. Artículo 1).

Los resultados obtenidos en los andamios de SG muestran que la concentración de los tres iones principales, Ca, P y Si, aumenta en el SFA en la primera parte del proceso. Sin embargo, la liberación de estos iones se realizó en menor proporción que en las muestras de BR. Este aumento en la concentración de dichos iones en el SFA va ligado a una disolución de una de las fases del andamio. Por otro lado, en la segunda parte del ensayo se puede observar un descenso evidente en las concentraciones de Ca y P. Dicho descenso se relaciona con la precipitación de la capa de HA en la superficie del material (Fig. 9. Artículo 2).

Nuestro objetivo fue comparar dos tipos de andamiajes elaborados a partir de dos métodos diferentes, pero con una misma composición química. Solo los andamios de BR presentaron la microestructura laminar típica de una composición eutectoide y que está compuesta por dos fases con diferentes ratios de degradación, mientras que los andamios de SG, debido a los productos de partida, presentaron un microestructura globular producida por una aglomeración de partículas aproximadamente cilíndricas. Este tipo de andamios podría ser un buen punto de inicio para el desarrollo de materiales de tercera generación. El tamaño de poro, su distribución y su nivel de porosidad necesitan estar equilibrados para poder guiar el crecimiento de hueso correctamente. Finalmente, estudios celulares se necesitan para evaluar la biocompatibilidad de los andamios.

6. CONCLUSIONES Y PROYECCIONES FUTURAS.

6.1 Conclusiones.

- Se ha producido un material cerámico de composición eutectoide (31 % en peso de TCP y 69% en peso de C₂S) dentro del sistema C₂S-TCP.
- Mediante la técnica de Réplica de Esponja Polimérica por inmersión de una esponja de PU en una suspensión de SG y BR se han obtenido andamios cerámicos 3D.
- Ambos procesos producen andamios con una misma macroporosidad (~95%) pero diferente microporosidad debido al número de recubrimientos realizados durante el procesado.
- Todos los andamios presentan una estructura jerarquizada, en cuanto al tamaño y distribución de poro, alcanzando la escala nanométrica.
- Los andamios obtenidos por BR presentan dos fases (α' -C₂S y Nurse's A) mientras que los andamios obtenidos por SG son multifásicos.
- Se desarrolló una microestructura laminar en el caso de los andamios obtenidos por BR y globular/granular en los andamios obtenidos por SG.
- Ambos andamios son bioactivos, pero con una cinética de reacción diferente. Los andamios de BR presentaron una bioactividad temprana (6h) mientras que los andamios de SG presentaron una bioactividad tardía (14). Estos resultados ponen de manifiesto que hay una relación entre la microestructura /composición química con el grado de bioactividad.
- Se ha analizado por IRTF la capa de precipitado presente en la superficie de ambos materiales, y se ha observado que dicha capa no es HA estequiométrico, sino que en realidad es de CHA debido a la presencia de grupos OH⁻ y CO₃²⁻. Los grupos CO₃⁻ sustituyen a los grupos PO₄³⁻ en la estructura cristalina del HA tratándose de una sustitución tipo B.
- La composición química, la estructura 3D y la microestructura del material desempeñan un papel fundamental en la cinética de reacción y, por tanto, en la bioactividad de los mismos.

6.2 Proyecciones Futuras.

- En este estudio hemos evaluado la bioactividad sumergiendo las muestras en SFA estático. Sin embargo, las condiciones reales del cuerpo humano no son estáticas. Los fluidos corporales son bombeados de manera continua, renovando el suministro de nutrientes y las concentraciones iónicas y eliminando las sustancias de desecho. Es por ello, que para recrear estas condiciones es necesario llevar a cabo el ensayo de bioactividad sumergiendo las muestras en SFA dinámico, con un flujo controlado y semejante al del interior del organismo, mediante, por ejemplo, el uso de una bomba peristáltica.
- Por otra parte, hay que realizar ensayos de biocompatibilidad *in vitro* mediante el uso de células madre mesenquimales humanas (CMM), cuya finalidad es determinar la capacidad del material para inducir la diferenciación celular hacia linajes osteogénicos, así como la capacidad de favorecer la adhesión celular en su superficie y la proliferación celular en su interior.
- Finalmente, es necesario realizar ensayos de biocompatibilidad *in vivo* mediante la implantación del material en un modelo animal adecuado.

7. BIBLIOGRAFÍA.

- ¹ Fernandez-Garcia M, Martinez J, Olmos JM, Gonzalez-Macias J, Hernandez JL. (2015). Review of the incidence of hip fracture in Spain. *Revista De Osteoporosis Y Metabolismo Mineral* 7(4):115-20.
- ² Agarwal R, Garcia AJ. Biomaterial strategies for engineering implants for enhanced osseointegration and bone repair. *Advanced Drug Delivery Reviews* 94:53-62.
- ³ <https://www.segg.es> (2017). Sociedad Española de Geratría y Gerontología.
- ⁴ Deng CJ, Chang J, Wu CT. (2019). Bioactive scaffolds for osteochondral regeneration. *Journal of Orthopaedic Translation* 17:15-25.
- ⁵ Lee K, Goodman SB. (2008). Current state and future of joint replacements in the hip and knee. *Expert Review of Medical Devices* 5(3):383-93.
- ⁶ Laurencin C, Khan Y, El-Amin SF. (2006). Bone graft substitutes. *Expert Review of Medical Devices* 3(1):49-57.
- ⁷ Hench LL. (2015). The future of bioactive ceramics. *Journal of Materials Science-Materials in Medicine* 26(2).
- ⁸ Bauer TW, Schils J. (1999). The pathology of total joint arthroplasty I. Mechanisms of implant fixation. *Skeletal Radiology* 28(8):423-32.
- ⁹ Kiradzhiyska DD, Mantcheva RD. (2019). Overview of Biocompatible Materials and Their Use in Medicine. *Folia medica* 61(1):34-40.
- ¹⁰ Hench LL. (1998). Biomaterials: a forecast for the future. *Biomaterials* 19(16):1419-23.
- ¹¹ Langer R, Vacanti JP. (1993). Tissue engineering. *Science* 260(5110):920-6.
- ¹² Hench LL, Polak JM. (2002). Third-generation biomedical materials. *Science*. 295(5557):1014.
- ¹³ Hench LL. (1991). Bioceramics - from concept to clinic. *Journal of the American Ceramic Society* 74(7):1487-510.
- ¹⁴ Jo J-I, Gao J-Q, Tabata Y. (2019). Biomaterial-based delivery systems of nucleic acid for regenerative research and regenerative therapy. *Regenerative therapy* 11:123-30.
- ¹⁵ Bains F, Novajra G, Vitale-Brovarone C. (2015). Bioceramics and Scaffolds: A Winning Combination for Tissue Engineering. *Frontiers in bioengineering and biotechnology* 3:202.

- ¹⁶ Bairo F, Novajra G, Miguez-Pacheco V, Boccaccini AR, Vitale-Brovarone C. (2016). Bioactive glasses: Special applications outside the skeletal system. *Journal of Non-Crystalline Solids* 432:15-30.
- ¹⁷ Miguez-Pacheco V, Hench LL, Boccaccini AR. (2015). Bioactive glasses beyond bone and teeth: Emerging applications in contact with soft tissues. *Acta Biomaterialia* 13:1-15.
- ¹⁸ Ratner BD, Bryant SJ. (2004). Biomaterials: Where we have been and where we are going. *Annual Review of Biomedical Engineering* 6:41-75.
- ¹⁹ Barrere F, van Blitterswijk CA, de Groot K. (2006). Bone regeneration: molecular and cellular interactions with calcium phosphate ceramics. *International Journal of Nanomedicine* 1(3):317-32.
- ²⁰ Cao WP, Hench LL. (1996). Bioactive materials. *Ceramics International* 22(6):493-507.
- ²¹ LeGeros RZ. (2002). Properties of osteoconductive biomaterials: Calcium phosphates. *Clinical Orthopaedics and Related Research* (395):81-98.
- ²² Bairo F, Vitale-Brovarone C. (2011). Three-dimensional glass-derived scaffolds for bone tissue engineering: Current trends and forecasts for the future. *Journal of Biomedical Materials Research Part A* 97(4):514-35.
- ²³ Fu Q, Saiz E, Rahaman MN, Tomsia AP. (2011). Bioactive glass scaffolds for bone tissue engineering: state of the art and future perspectives. *Materials Science & Engineering C-Materials for Biological Applications* 31(7):1245-56.
- ²⁴ Owen GR, Dard M, Larjava H. (2018) Hydroxyapatite/beta-tricalcium phosphate biphasic ceramics as regenerative material for the repair of complex bone defects. *Journal of Biomedical Materials Research Part B-Applied Biomaterials* 106(6):2493-512.
- ²⁵ Tite T, Popa A-C, Balescu LM, Bogdan IM, Pasuk I, Ferreira JMF, et al. (2018) Cationic Substitutions in Hydroxyapatite: Current Status of the Derived Biofunctional Effects and Their In Vitro Interrogation Methods. *Materials* 11(11).
- ²⁶ Otsuki B, Takemoto M, Fujibayashi S, Neo M, Kokubo T, Nakamura T. (2006) Pore throat size and connectivity determine bone and tissue ingrowth into porous implants: Three-dimensional micro-CT based structural analyses of porous bioactive titanium implants. *Biomaterials* 27(35):5892-900.
- ²⁷ Rabadan-Ros R, Velasquez PA, Meseguer-Olmo L, De Aza PN. (2016) Morphological and Structural Study of a Novel Porous Nurse's A Ceramic with Osteoconductive Properties for Tissue Engineering. *Materials (Basel, Switzerland)* 9(6).

- ²⁸ De Aza AH, Velasquez P, Alemany MI, Pena P, De Aza PN. (2007). In situ bone-like apatite formation from a Bioeutectic((R)) ceramic in SBF dynamic flow. *Journal of the American Ceramic Society* 90(4):1200-7.
- ²⁹ Bruzauskaite I, Bironaite D, Bagdonas E, Bernotiene E. (2016) Scaffolds and cells for tissue regeneration: different scaffold pore sizes-different cell effects. *Cytotechnology* 68(3):355-69.
- ³⁰ Rodrigues AI, Reis RL, van Blitterswijk CA, Leonor IB, Habibovic P. (2017). Calcium phosphates and silicon: exploring methods of incorporation. *Biomaterials research* 21:6.
- ³¹ Gibson IR, Hing KA, Revell PA, Santos JD, Best SM, Bonfield W. (2002). Enhanced in vivo response to silicate-substituted hydroxyapatite. *Bioceramics* 14 218-2:203-6.
- ³² Ros-Tarraga P, Mazon P, Rodriguez MA, Meseguer-Olmo L, De Aza PN. (2016). Novel Resorbable and Osteoconductive Calcium Silicophosphate Scaffold Induced Bone Formation. *Materials* 9(9).
- ³³ R. W. Nurse, J. H. Welch, W. Gutt. (1959). High-Temperature Phase Equilibria in the System Dicalcium Silicate-Tricalcium Phosphate. *Journal of the chemical Society*.
- ³⁴ W. Fix, H. Heyman, R. Heinke. (1969). Subsolidus Relations in System $2\text{CaO}\cdot\text{SiO}_2 - 3\text{CaO}\cdot\text{P}_2\text{O}_5$. *Journal of the American Ceramic Society*. Vol. 52.
- ³⁵ Rubio V, de la Casa-Lillo MA, De Aza S, De Aza PN. (2011). The System $\text{Ca}_3(\text{PO}_4)_2 - \text{Ca}_2\text{SiO}_4$: The Sub-System $\text{Ca}_2\text{SiO}_4 - 7\text{CaO}\cdot 2\text{P}_2\text{O}_5 \cdot 2\text{SiO}_2$. *Journal of the American Ceramic Society* 94(12):4459-62.
- ³⁶ Martinez IM, Velasquez PA, De Aza PN. (2010). Synthesis and stability of alpha-tricalcium phosphate doped with dicalcium silicate in the system $\text{Ca}_3(\text{PO}_4)_2 - \text{Ca}_2\text{SiO}_4$. *Materials Characterization* 61(7):761-7.
- ³⁷ Ros-Tarraga P, Mazon P, Meseguer-Olmo L, De Aza PN. (2016). Revising the Subsystem Nurse's A-Phase-Silicocarnotite within the System $\text{Ca}_3(\text{PO}_4)_2 - \text{Ca}_2\text{SiO}_4$. *Materials* 9, 322.
- ³⁸ Liu X, Morra M, Carpi A, Li B. (2008). Bioactive calcium silicate ceramics and coatings. *Biomedicine & Pharmacotherapy* 62(8):526-9.
- ³⁹ Gou ZG, Chang J, Zhai WY, Wang JY. (2005). Study on the self-setting property and the in vitro bioactivity of beta- Ca_2SiO_4 . *Journal of Biomedical Materials Research Part B-Applied Biomaterials* 73B (2):244-51.
- ⁴⁰ R.G. Carrodeguas, S. De Aza. (20011). α -Tricalcium phosphate: Synthesis, properties and biomedical applications. *Acta Biomaterialia* 7:3536-3546.

- ⁴¹ Eliaz N, Metoki N. (2017). Calcium Phosphate Bioceramics: A Review of Their History, Structure, Properties, Coating Technologies and Biomedical Applications. *Materials* 10(4).
- ⁴² Kokubo T, Takadama H. (2006). How useful is SBF in predicting in vivo bone bioactivity?. *Biomaterials*. 27(15):2907-15.
- ⁴³ Kolk A, Handschel J, Drescher W, Rothamel D, Kloss F, Blessmann M, Heiland. M, Wolf. K.D, Smeets, R. (2012). Current trends and future perspectives of bone substitute materials - From space holders to innovative biomaterials. *Journal of Cranio-Maxillofacial Surgery* 40(8):706-18.
- ⁴⁴ A.J. Salinas, P.Esbirt, M. Vallet-Regí. (2013). A tissue engineering approach based on the use of bioceramics for bone repair. *Biomaterials Science*.1:40-51.
- ⁴⁵ Parrilla-Almansa A, Garcia-Carrillo N, Ros-Tarraga P, Martinez CM, Martinez-Martinez F, Meseguer-Olmo L, et al. (2018). Demineralized Bone Matrix Coating Si-Ca-P Ceramic Does Not Improve the Osseointegration of the Scaffold. *Materials* 11(9).
- ⁴⁶ De Aza PN, Rodriguez MA, Gehrke SA, Mate-Sanchez de Val JE, Calvo-Guirado JL. (2017). A Si-alpha TCP Scaffold for Biomedical Applications: An Experimental Study Using the Rabbit Tibia Model. *Applied Sciences-Basel* 7(7).
- ⁴⁷ Bruzauskaite I, Bironaite D, Bagdonas E, Bernotiene E. (2016). Scaffolds and cells for tissue regeneration: different scaffold pore sizes-different cell effects. *Cytotechnology* 68, 355-369.
- ⁴⁸ Rubio V, Mazon P, de la Casa-Lillo MA, De Aza PN. (2015). Preparation, characterization and in vitro behavior of a new eutectoid bioceramic. *Journal of the European Ceramic Society* 35(1):317-28.
- ⁴⁹ Bobbert FSL, Zadpoor AA. (2017). Effects of bone substitute architecture and surface properties on cell response, angiogenesis, and structure of new bone. *Journal of Materials Chemistry B* 5(31):6175-92.
- ⁵⁰ Murphy CM, Haugh MG, O'Brien FJ. (2010). The effect of mean pore size on cell attachment, proliferation and migration in collagen-glycosaminoglycan scaffolds for bone tissue engineering. *Biomaterials* 31(3):461-6.
- ⁵¹ Li X, van Blitterswijk CA, Feng Q, Cui F, Watari F. (2008). The effect of calcium phosphate microstructure on bone-related cells in vitro. *Biomaterials* 29(23):3306-16.
- ⁵² Lew K-S, Othman R, Ishikawa K, Yeoh F-Y. (2012). Macroporous bioceramics: A remarkable material for bone regeneration. *Journal of Biomaterials Applications* 27(3):345-58.

- ⁵³ Gauthier O, Bouler JM, Aguado E, Pilet P, Daculsi G. (1998). Macroporous biphasic calcium phosphate ceramics: influence of macropore diameter and macroporosity percentage on bone ingrowth. *Biomaterials* 19(1-3):133-9.
- ⁵⁴ Hadjicharalambous C, Prymak O, Loza K, Buyakov A, Kulkov S, Chatzinikolaidou M. (2015). Effect of Porosity of Alumina and Zirconia Ceramics toward Pre-Osteoblast Response. *Frontiers in bioengineering and biotechnology* 3:175.
- ⁵⁵ Fleisch H, Bisaz S. (1962). Mechanism of calcification - inhibitory role of pyrophosphate. *Nature* 195(4844):91.
- ⁵⁶ Fleisch H, Russel RGG, Straumann F. (1966). Effect of pyrophosphate on hydroxyapatite and its implications in calcium homeostasis. *Nature*. 212(5065):901.
- ⁵⁷ Terkeltaub RA. (2001). Inorganic pyrophosphate generation and disposition in pathophysiology. *American Journal of Physiology-Cell Physiology* 281(1):C1-C11.
- ⁵⁸ Padilla S, Roman J, Sanchez-Salcedo S, Vallet-Regi M. (2006). Hydroxyapatite/SiO₂-CaO-P₂O₅ glass materials: In vitro bioactivity and biocompatibility. *Acta Biomaterialia* 2(3):331-42.
- ⁵⁹ Karamian E, Nasehi A, Saber-Samandari S, Khandan A. (2017). Fabrication of hydroxyapatite-baghdadite nanocomposite scaffolds coated by PCL/Bioglass with polyurethane polymeric sponge technique. *Nanomedicine Journal* 4(3):177-83.
- ⁶⁰ Novotna L, Kucera L, Hampl A, Drdlik D, Cihlar J, Jr., Cihlar J. (2019). Biphasic calcium phosphate scaffolds with controlled pore size distribution prepared by in-situ foaming. *Materials Science & Engineering C-Materials for Biological Applications* 95:363-70.

8. ANEXO: COMPENDIO DE ARTICULOS

Artículo 1

Rightslink® by Copyright Clearance Center

<https://s100.copyright.com/AppDispatchServlet#formTop>



RightsLink®



Home



Help



Email Support



Sign in



Create Account



Eutectoid dicalcium silicate-Nurse's A ceramic scaffold: Processing and in vitro bioactivity

Author: C. Navalón, P. Mazón, P.N. De Aza

Publication: Ceramics International

Publisher: Elsevier

Date: 1 December 2019

© 2019 Elsevier Ltd and Techna Group S.r.l. All rights reserved.

Please note that, as the author of this Elsevier article, you retain the right to include it in a thesis or dissertation, provided it is not published commercially. Permission is not required, but please ensure that you reference the journal as the original source. For more information on this and on your other retained rights, please visit: <https://www.elsevier.com/about/our-business/policies/copyright#Author-rights>

BACK

CLOSE WINDOW

© 2020 Copyright - All Rights Reserved | [Copyright Clearance Center, Inc.](#) | [Privacy statement](#) | [Terms and Conditions](#)
Comments? We would like to hear from you. E-mail us at customercare@copyright.com



Eutectoid dicalcium silicate-Nurse's A ceramic scaffold: Processing and *in vitro* bioactivity

C. Navalón^{a,*}, P. Mazón^b, P.N. De Aza^a

^a Instituto de Bioingeniería, Universidad Miguel Hernández, Avda. Ferrocarril s/n, 03202, Elche, Alicante, Spain

^b Departamento de Ciencia de Materiales, Óptica y Tecnología Electrónica. Universidad de Miguel Hernandez, Avda. De la Universidad s/n, 03202, Elche, Alicante, Spain

ARTICLE INFO

Keywords:

A-powders: solid state reaction
B-Microstructure-final
D-silicate
E-Biomedical applications
Calcium silicate

ABSTRACT

The aim of this research was the processing, characterisation and *in vitro* bioactivity of a novel ceramic 3D porous scaffold to be used in the bone tissue engineering field. A calcium silicophosphate scaffold, with nominal composition 31 wt% tricalcium phosphate (TCP-3CaO-P₂O₅)-69 wt% dicalcium silicate (C₂S-2CaO-SiO₂), was produced by the polymer sponge replica method. The scaffold was analysed by Scanning Electron Microscopy (SEM), X-Ray Diffraction (XRD), Fourier Transform Infrared Spectrometry (FTIR) and Hg porosimetry techniques. The results indicated that the biphasic porous Si-Ca-P scaffolds presented a lamellar microstructure of alternating α'-C₂S and α - TCP phases and an interconnected porous network (95 ± 3%), with a hierarchical distribution in pore size terms (55.12 nm–600 μm). The scaffold displayed good and fast bioactivity, which was confirmed by the presence of CHA on its surface after being immersed 6 h in simulated body fluid (SBF) according to Kokubo guidelines. These results confirm that the scaffold is suitable for bone tissue engineering.

1. Introduction

Today's life expectancy has increased considerably due to health advances. In spite of this progress enhancing people's quality of life and longevity, it also increases the incidence of problems related to bone and joint degeneration, such as fractures, osteoporosis, bone metastasis, etc., in older people with diminished bone regeneration capacity. This means that 50% of chronic patients in developed countries aged more than 50 years will suffer bone problems [1,2].

Traditionally, these bone injuries have been treated by reconstructive surgery using autologous, allogeneic or xenogeneic implants, which involve restrictions such as bone tissue availability or immunological responses. Given these disadvantages, the need to develop a new discipline such as tissue engineering came about, which is able to create new treatments and techniques for bone tissue regeneration. This discipline advances towards the creation of a new kind of biomaterials with good bioactivity and excellent mechanical properties. In general terms, the ideal scaffold should be designed to provide temporal support by inducing bone regeneration and promoting cell and molecular stimuli in a controlled manner, while the scaffold reabsorbs itself [2–8].

A large scaffold surface area mimics the human cancellous bone structure to promote good adhesion of biological tissue cells and new bone phase growth. Porosity is important for promoting cellular

migration from bone tissue to the internal scaffold area. Although no consensus has been reached by authors about an optimal pore size, it is well-established as a general rule that pores below 10 μm provide a larger surface area for the natural bone-implant interaction, protein adsorption, ion exchange and new bone formation [9,10]. Pores around 100 μm improve the initial adhesion of osteoblasts and allow their migration to the biomaterial [11], but larger pores (> 300 μm) are needed to improve new bone formation [12,13]. Highlight, porosity also allows vascular network growth through the material, supplying nutrients to the cells growing inside it. These characteristics allow the scaffold to be integrated into the damaged bone involved [14].

A wide variety of techniques have been used to produce 3D scaffolds: solvent casting/particulate leaching [15], gas foaming [16], emulsification freeze-drying [17], phase separation [18], electrospinning [19], 3D printing [20] and polymer sponge replica [2].

In the present study, ceramic 3D scaffolds were prepared by the polymer sponge replica method in accordance with the eutectoid composition reported in the literature [21]. Despite it not being a novel technique compared to current ones, the sponge replica method offers advantages such as: it is a low-cost technique that allows ceramics with a controllable pore size and an interconnected porous network, and porous ceramics with good thermal properties and high resistance to chemical attacks, to be obtained. It is a versatile technology as porous ceramics properties can be molded by only modifying some slurry

* Corresponding author. Instituto de Bioingeniería, Universidad Miguel Hernandez, 03202, Elche, Alicante, Spain.

E-mail addresses: carlos.navalon@goumh.umh.es, cnavalon92.cnd@gmail.com, piedad@umh.es (C. Navalón), pmazon@umh.es (P. Mazón).

<https://doi.org/10.1016/j.ceramint.2019.07.172>

Received 10 June 2019; Received in revised form 12 July 2019; Accepted 15 July 2019

Available online 15 July 2019

0272-8842/ © 2019 Elsevier Ltd and Techna Group S.r.l. All rights reserved.

variables [22,23].

Synthetic 3 D scaffolds with eutectoid composition (31 wt% tricalcium phosphate (TCP-3CaO·P₂O₅)-69 wt% dicalcium silicate (C₂S-2CaO·SiO₂)) were developed. Ceramics were studied in-depth to manufacture bioactive and biodegradable scaffolds with structural and microstructural optimised properties. These properties were also tested under *in-vitro* conditions in SBF. To our knowledge, there are no studies about porous scaffolds with a eutectoid composition.

2. Material and methods

2.1. Materials and processing methods

The chemicals used in the ceramic powder synthesis were the following oxides: calcium hydrogen phosphate anhydrous (CaHPO₄ > 98.0 wt%, Acros), calcium carbonate (CaCO₃ > 99.0 wt%, Acros) and silicon oxide (SiO₂ > 99.7 wt%, Stream Chemicals). Chemicals were mixed according to the stoichiometry of the eutectoid composition (31 wt% TCP-69 wt% C₂S) and homogenised with acetone as suspension media and powder was cold isostatically pressed at 1400 bar.

The green bars were put in a platinum crucible and heated for 6 h at 1500 °C. Then they were liquid nitrogen quenched by being rapidly withdrawn from the furnace. The obtained material was ground in a laboratory miller (MM301-Retsch) using PSZ-zirconia balls and isopropyl alcohol as suspension media. After the milling process, powder was cold isostatically pressed and heated up to 1550 °C, and kept at 1550 °C for 3 h with a subsequent annealing step at 512 °C, 5 °C below the invariant temperature. Once the final ceramic material had been obtained, it was ground for different times by a mill (PM100-Retsch) and its particle size was measured by laser diffraction (Mastersizer2000E Device-Malvern).

2.2. Creation of ceramic 3D porous scaffolds

Ceramic slurry was prepared by mixing the final ceramic material with deionised water, and by adding Dolapix CE 64 (Zschimmer & Schwarz) and Optapix PAF 35 (Zschimmer & Schwarz) to achieve the proper rheological features.

A polyurethane sponge (Ø 1 cm, height 0.7 cm) was immersed 3 times in the resultant slurry to obtain a thick enough structure to hold the scaffold's weight. Any excess material was removed by squeezing the sponge and pores were opened using compressed air to ensure that no pores closed. After coating, the 3D scaffolds were dried at room temperature and heated up to 1550 °C, left at this temperature for 3 h, followed by slow cooling to 512 °C, keeping at this temperature for 24 h. The resultant scaffold had an Ø of 0.9 cm and was 0.6 cm high.

2.3. Characterisation of ceramic 3D porous scaffolds

The mineralogical characterisation was carried out by X-Ray diffraction (XRD) (Bruker-AXS D8Advance automated diffractometer) to determine crystalline phases using CuK_α 1.2 radiation (1.54056 Å). Data were collected in the Bragg-Brentano(θ/2θ) vertical geometry. Phases were identified by the database provided by the crystallography open database (COD).

The sample porosity and pore size distribution for the scaffold were determined by mercury porosimetry in a Poremaster-60 GT (Quantachrome Instruments, Boyton Beach, FL, USA) within the 13.789 Bar to 4102.24 Bar pressure range, which corresponds to a pore diameter range between 1068.82 µm and 0.003585 µm. Three samples (~0.8 g) were analysed by this technique. One more sample was also used in each case if the obtained porosity values differed by more than 5%. He picnometry (Quantachrome Instruments, Boyton Beach, FL, USA) was done to establish the sample's density.

The material's microstructure and its pore size (5 samples/20

measures per sample) were characterised by Scanning Electron Microscopy fitted with an Energy-Disperse X-Ray spectroscopy (SEM-EDS, SEM-Hitachi S-3500 N and INCA system, by Oxford Instruments Analytical, UK, respectively) by coating samples with palladium.

Finally, to know the scaffolds' chemical bond composition, Fourier Transform Infrared Spectrometry (ATR-FTIR, Thermo SCIENTIFIC Nicolet iS5 equipped with an iDR ATR accessory) was utilised.

2.4. Bioactivity analysis

Bioactivity was checked for several time periods according to the protocol suggested by Kokubo [24] who, in 2006, proposed Tris-Buffered SBF with an ion concentration that almost equalled human blood plasma. Scaffolds were placed into falcon tubes (50 ml) for several time periods (from 3 h to 21 days), and they were incubated at 37°C ± 0.5°C in a shaking water bath. Samples were removed from SBF for each tested assay time and their bioactivity were observed by SEM-EDS. The remaining SBF was used to determine the Si, Ca, P ion concentrations by inductively Coupled Plasma Optical Emission Spectrometry (ICP-OES PerkinElmer Optima 2000™) [25].

Finally, an ATR-FTIR was performed using the same equipment as that mentioned above to determine the chemical bond composition of the new Ca-P precipitate present in the outside and inside scaffold area after being soaked in SBF for 21 days.

3. Results

3.1. Characterisation of ceramic powder

The ceramic powder obtained after proper heat treatment was mineralogically characterised by XRD (Fig. 1) and showed a mixture of two crystalline phases: α'-C₂S (COD card no. 96-210-3317) and Nurse's A Phase (COD card no. 00-011-0676). The diffraction peaks were slightly displaced in relation to the cited cards as both phases were solid solutions. The displacement was 0.1° for α'-C₂S and 0.3° for Nurse's A phase. These two phases agreed with the composition corresponding to the eutectoid point, 31 wt% TCP-69 wt% C₂S, as described in the literature [21]. No other crystalline phases were observed.

In order to create 3D scaffolds by the polymer sponge replica method, it was necessary to use the smallest and narrowest particle size distributions. Bearing in mind these requirements, the ceramic was milled with PSZ-zirconia balls for different time periods (Fig. 2 A). The best milling time was 2 h (pink line) due to its narrow and small particle size distribution, which showed an average particle size of 13.76 µm in the 50% sample volume. A XRD analysis was also performed to assess possible crystallinity loss due to milling (Fig. 2 B). Slight differences in the crystalline degree were observed with increasing milling times. Consequently, the background increased and some peaks disappeared. These effects became more evident 1.5 h after milling.

3.2. Characterisation of ceramic 3D scaffolds

Fig. 3 A, B, shows the ceramic 3D scaffold after the sintering treatment and presented a similar open porous structure to the polyurethane sponge template in spite of an average shrinkage of 37.3%. The XRD run with the ceramic 3D scaffold (Fig. 3 C.) did not show any extra phase, but slight crystallinity loss was detected due to the minor increase in the background.

The SEM micrographs of the ceramic 3D scaffolds were taken for the microstructural characterisation. An interconnected porous structure (Fig. 4 A) with a pore size ratio between 300 µm and 600 µm was observed. The ceramic 3D scaffolds were chemical-etched with acetic acid 1% for 60 s to observe the characteristic morphology of a eutectoid material. Fig. 4 B-D shows the 3D scaffold at different magnifications and exhibits a specific surface topography. This topography corresponds to an irregular lamellar morphology, which is typical of the

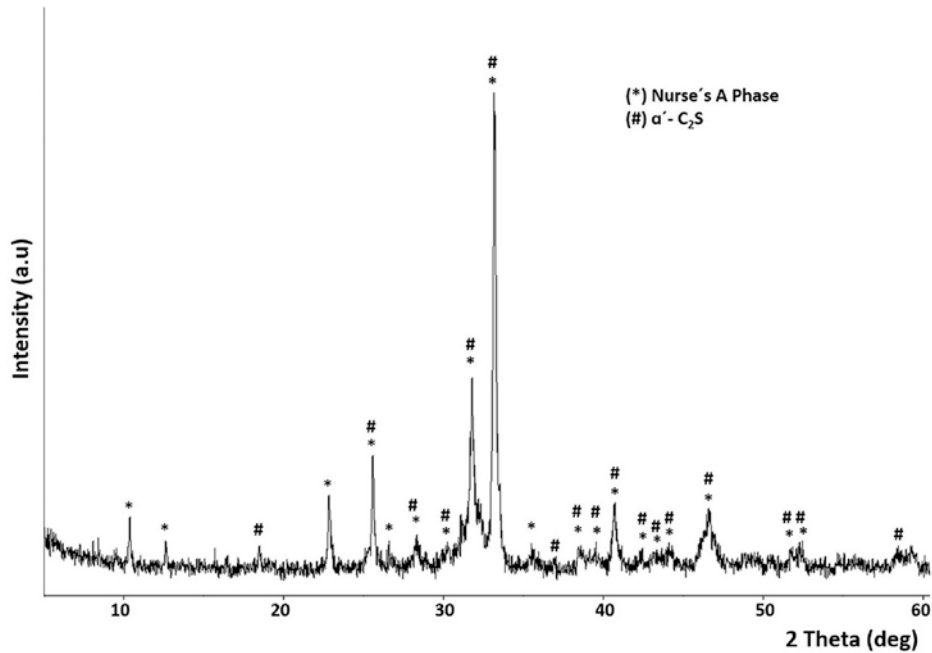


Fig. 1. The XRD pattern of the ceramic composition, (*) Nurse's A phase and (#) α' -C₂S.

eutectoid invariant point. According to the XRD, this lamellar morphology corresponds to dicalcium silicate and Nurse's A phase phases (Fig. 3C). The two phases were so intimately mixed that it was impossible to distinguish between them by EDS (Fig. 4 E).

The scaffold's chemical bond characterisation was made by ATR-FTIR (Fig. 5). The spectra of silicates and phosphates were characterised by the SiO_4^{2-} and PO_4^{3-} tetrahedral units. In fact, these groups presented similar vibrational modes given their similarities in terms of the tetrahedral molecular units [13]. As Fig. 5 depicts, there

are two zones with significant absorption bands. The first corresponds to the bands between 500 and 600 cm^{-1} and the second to the bands between 870 and 1300 cm^{-1} . In the first zone, the presence of bands corresponding to 515 , 538 and 584 cm^{-1} belong to the bend vibrational mode of the PO_4^{3-} groups. In the second zone, Si–O–Si bending at 873 cm^{-1} , Si–O–Si/ PO_4^{3-} symmetrical stretching at 906 cm^{-1} , Si–O–Si stretching between 1080 and 1100 cm^{-1} and PO_4^{3-} asymmetrical stretching between 1000 and 1300 cm^{-1} were identified [26]. Note that the absorption bands corresponding to the second spectra

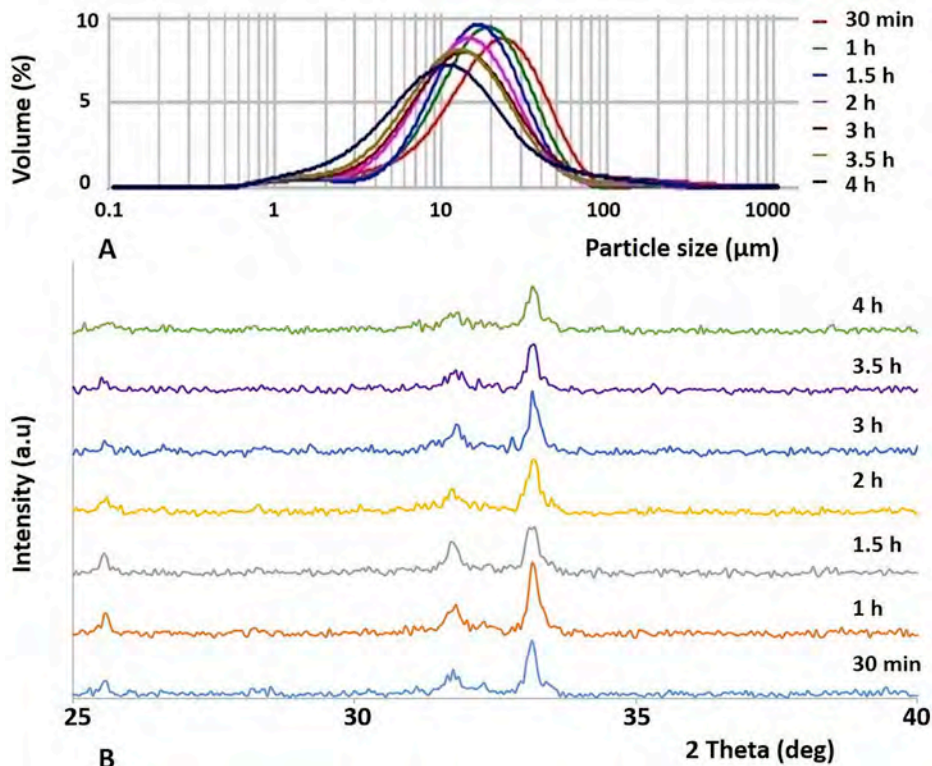


Fig. 2. (A) Particle size and (B) the XRD analysis for the different milling times.

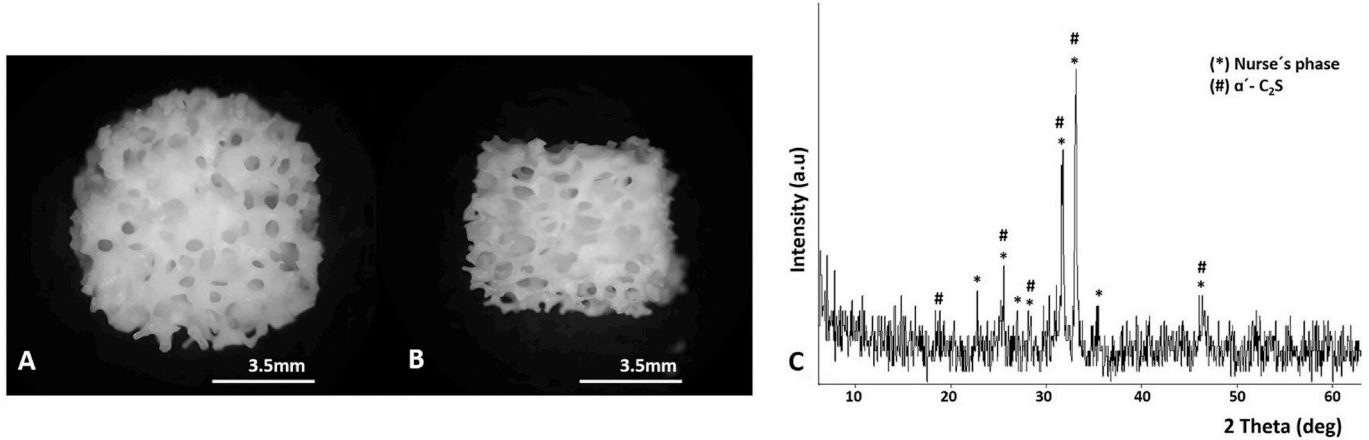
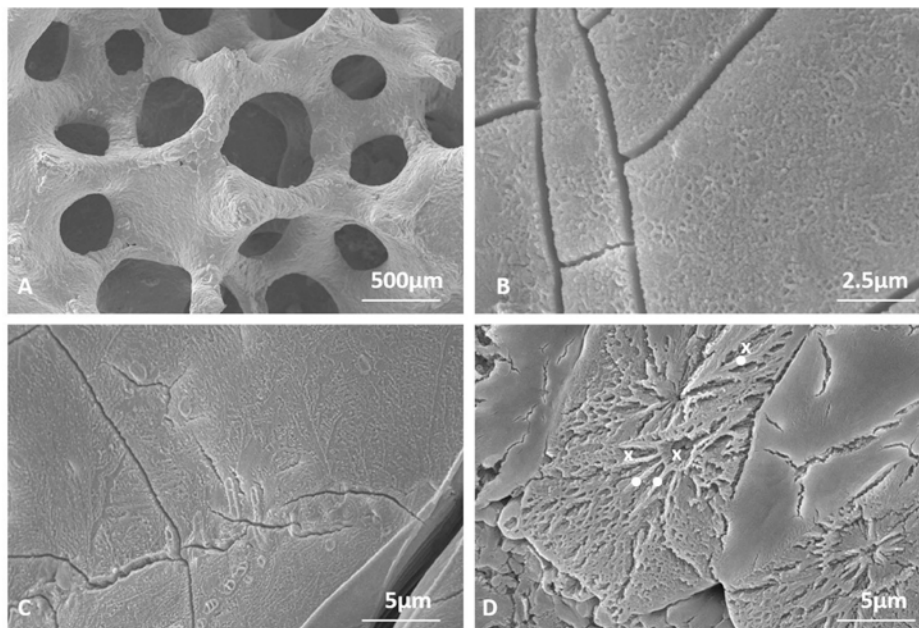


Fig. 3. (A, B) Optical micrographs of the ceramic 3D scaffolds and (C) the XRD of the Ceramic 3D scaffold.

zone overlap.

When a granular porous material is analysed by mercury porosimetry, two kind of empty spaces can be detected: those corresponding to the empty spaces among particles, known as interparticle spaces, and those corresponding to the empty spaces of the particles themselves, called intraparticle spaces. By looking at Fig. 6 A, the intrusion profiles showed significant mercury penetration into pores between 65.8 μm and 28.3 μm, and minor mercury penetration between 1.02 μm and 0.049 μm. The pore size range is represented more clearly

in Fig. 6 B, where we can see many pores that might mimic cancellous bone (51.28 μm) and nanometer-sized pores (from 91 nm to 55.12 nm). The first mercury intrusion corresponds to the filling of the interparticle spaces, which results in interparticle porosity of 8.76%, while the following mercury intrusion corresponds to the filling of intraparticle spaces, which results in an intraparticle porosity of 4.07%. To summarise, we can state that the scaffold presents a total strud porosity of 12.83%, and a total macroporosity (determined by the Archimedes method) of 95%. All the physical results are summarised in Table 1.



EDS Microanalysis of inner figure 4 D

Zone	Atomic %		
	Ca	P	Si
x	69.73	16.76	13.51
*	63.36	20.13	16.50

Fig. 4. SEM micrographs showing (A) the porous network, (B–D) detailed surface topography and (E) the EDS microanalysis.

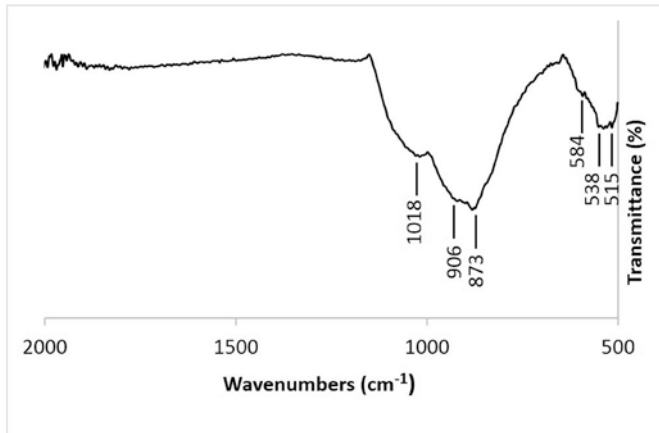


Fig. 5. The ATR-FTIR spectra of the ceramic 3 D scaffold.

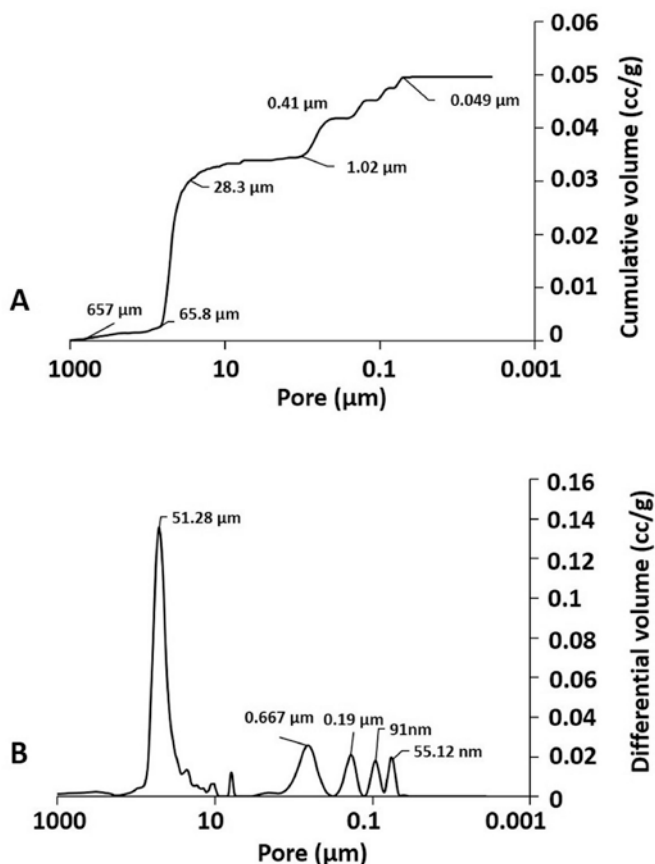


Fig. 6. Mercury intrusion curves (A) cumulative intruded volume versus pore diameter and (B) differential-intruded volume versus pore diameter.

3.3. The SBF *in vitro* test

The scaffold's bioactivity was analysed by soaking samples from 3 h to 21 days in SBF, which was prepared according to the protocol

Table 1
Summary data from the porosimetry test.

Macroporosity (%)	Total strud porosity (%)	Interparticle porosity (%) ^a	Intraparticle porosity (%) ^b	Apparent density (g/cc)	Surface area (m ² /g)
95	12.83	8.76	4.07	2.58	0.36

^a Corresponding to pores < 1 μm.

^b Corresponding to 1 μm < 300 μm.

proposed by Kokubo in 2006 [24]. A large part of the scientific community has recognised this assay to be a valuable method for the preliminary assessment of biomaterials bioactivity [12,27,28]. The results from 6 h to 5 d are shown in Fig. 7. A surface analysis was carried out by SEM-EDS to evaluate the scaffold's bioactivity, which is characterised by the Ca–P precipitated formation on the scaffold surface when it came into contact with SBF. At the beginning of the assay (1 d), the Ca/P ratio measured by EDS was $1.45 < \text{Ca/P} < 1.6$ and was $1.65 < \text{Ca/P} < 1.75$ at the end of the assay (21 d). In this way, we conclude that the Ca–P precipitate was apatite-like.

As shown in Fig. 7 A, the ceramic 3D scaffold surface was covered by isolated apatite-like spheres at 6 h. At 1 d, the material's surface was completely covered by apatite-like (Fig. 7 B, bottom) and started to close the micropores due to the continuous precipitation of apatite-like around them (Fig. 7 B, upper). Yet despite continuous precipitate growth, the 3D macropores structure remained unchanged, as shown at 3 d (Fig. 7C, upper). From this time point (3 d), microcracks appeared due to the air-dried samples, which indicates thick apatite layer deposition (Fig. 7C, bottom). Finally, apatite-like thickness increased with longer exposure times in SBF (5 d), as shown in Fig. 7 D (bottom). This increased thickness was due to the continuous apatite-like deposition over the sample surface, which took place layer by layer.

The bioactivity study was prolonged until 21 d to complete the established immersion times ending the full test. These data (7 d–21 d) are not shown in Fig. 7 because the morphology observed at 5 d (Fig. 7 D) remained until the assay ended. The results obtained at 3 h are not shown in Fig. 7 as the eutectoid material's lamellar microstructure remained unchanged and no precipitation was detected (Fig. 4B–D).

An ATR-FTIR of the 21-day sample (both outside and inside) was performed to determine if SBF flowed through the interconnected porous network and reached all the scaffold zones. It was also performed to establish the apatite type that precipitated over the scaffold surface (Fig. 8).

The infrared spectra showed the presence of precipitate in both sample areas (Fig. 8 B). The spectra before (Fig. 5) and after SBF (Fig. 8 B) presented coincidences according to the PO_4^{3-} groups and the silicate network. They showed intensive IR absorption bands at different ratios: $560\text{--}600\text{ cm}^{-1}$ corresponding to PO_4^{3-} double flexion and $1000\text{--}1300\text{ cm}^{-1}$ corresponding to PO_4^{3-} asymmetrical stretching. Regrettably, the bands between 1080 and 1100 cm^{-1} that corresponded to the silicate network could not be distinguished because the PO_4^{3-} groups overlapped. However, a peak corresponding to the silicate network was detected at 872 cm^{-1} in the inside scaffold part (Fig. 8 B, red spectra). This peak was also detected before SBF (Fig. 5.), but was not found in the outside scaffold part, which suggests that in the inside scaffold area remained a phase containing Si.

New bands related to the presence of OH^- groups were found in the inside and outside scaffold areas (Fig. 8 B). The first was found at $1633\text{ cm}^{-1}/1635\text{ cm}^{-1}$ and the second at $3396\text{ cm}^{-1}/3332\text{ cm}^{-1}$ [29–31]. Finally, other new bands related to the CO_3^{2-} groups were detected between 1460 and 1530 cm^{-1} in both scaffold areas, which indicates that the apatite-like is actually carbonate-hydroxyapatite (CHA).

An ICP-OES test was needed to observe the Ca, P and Si ion concentration changes in the SBF measured at the different soaking times (Fig. 9). The ceramic 3D scaffold releases silicon and calcium ions, which increases the concentrations in SBF. This behaviour may be

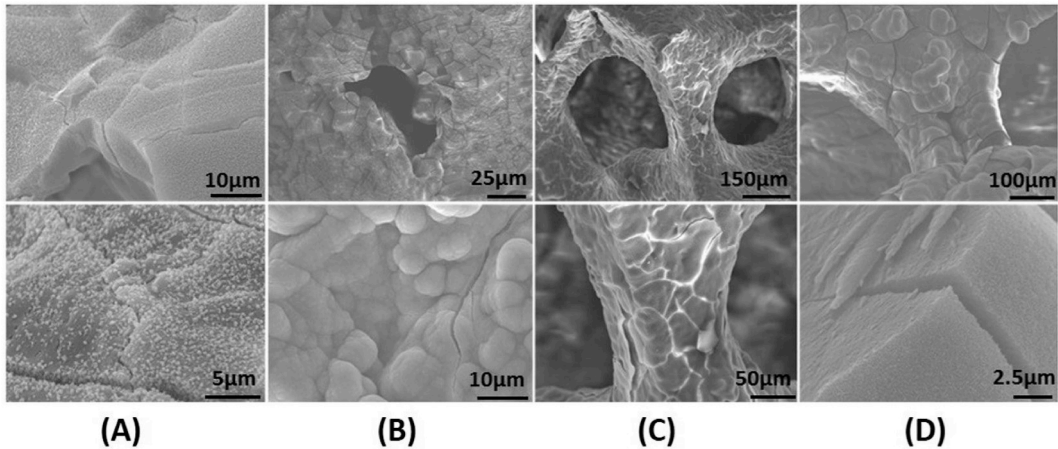


Fig. 7. SEM micrographs of the ceramic 3 D scaffolds after soaking in SBF for (A) 6 h, (B) 1 d, (C) 3 d and (D) 5 d at low (upper micrographs) and high (bottom micrographs) magnifications.

related to the scaffold dissolution. Furthermore, during certain time periods, calcium ions were removed from the media in parallel with phosphorous ions, which underwent a gradual ion concentration decrease. These changes indicate the formation of a precipitate on the scaffold surface. Finally, the marked increase in the concentration of Ca ions between 14 d and 21 d may be related to the precipitate-layer dissolution. This might happen given the large amount of precipitate on the scaffold surface. This precipitate is mechanically unstable and, consequently, breaks off from the structure and dissolves in the SBF.

4. Discussion

Bone tissue engineering is continuously being developed and the creation of biosynthetic bone substitutes is enhanced, which may elude the need to use autologous bone tissue [32]. Advances in this discipline generate new kind of structures that are able to repair, restore and regenerate bone tissue to a healthy state. An ideal 3D scaffold must have similar structure and mechanical properties to bone tissue, and be osteoinductive, osteoconductive and osteogenetic at the same time. It must also degrade over time into non-toxic products, which can be metabolised as the scaffold acts as a temporary support.

Materials bioactivity can be improved by adding inorganic elements to scaffolds, as previously reported in bio-glass or bio-ceramics

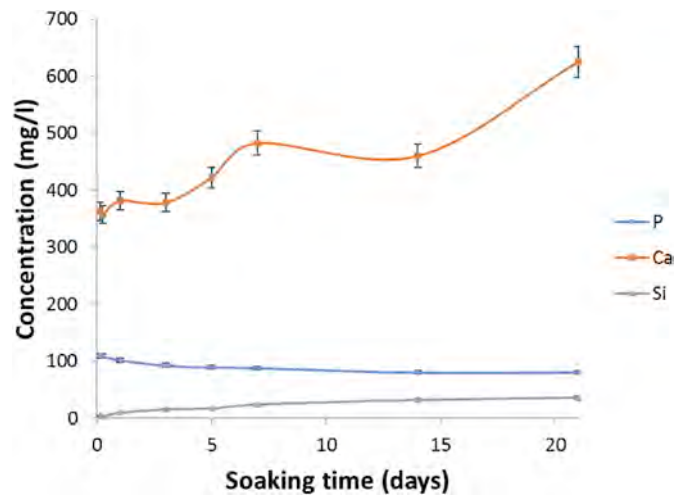


Fig. 9. Changes in the calcium (Ca, Orange, ■), phosphorous (P, Blue, ●), and silicon (Si, Grey, ▲) ion concentrations with soaking times in SBF solution.

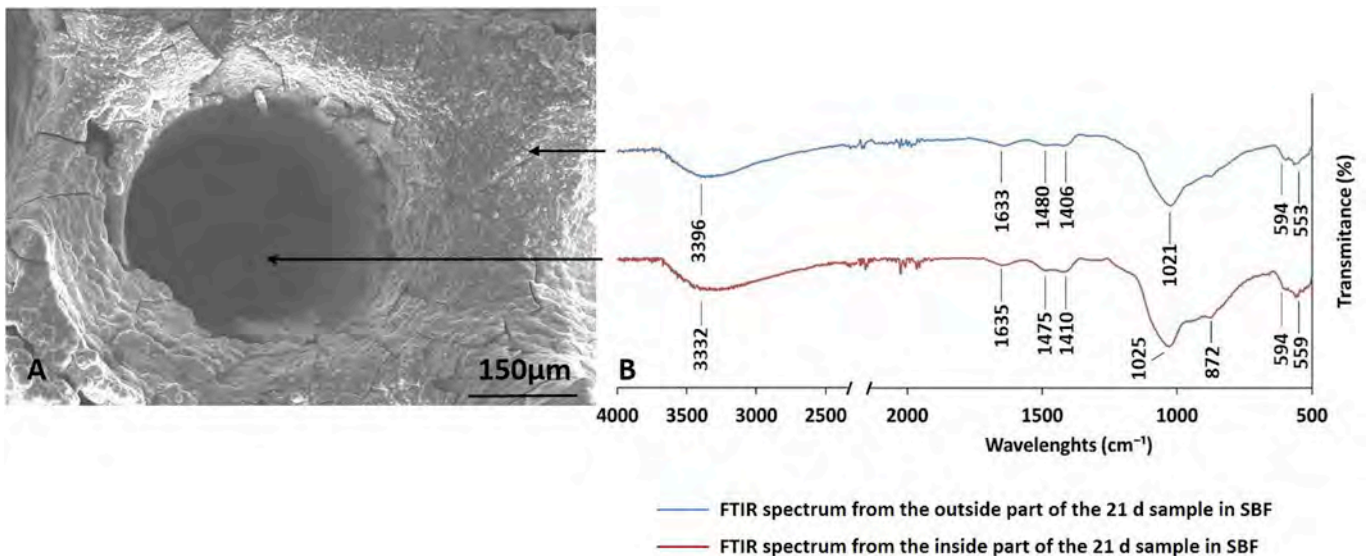


Fig. 8. SEM micrograph at (A) 21 d and (B) ATR-FTIR spectra from the outside and inside part of the 21 d SBF soaked sample.

containing CaO, SiO₂, and P₂O₅ [33,34]. However, scaffold composition is not enough to act as an excellent bone tissue engineering candidate because it must have a network of interconnected pores to develop the scaffold's full potential as a bone regenerating material. The presence of this network is of critical importance because it will modulate the bone formation process by controlling nutrient supply, waste cellular products circulation, angiogenesis, close contact with cells, and bone tissue in-growth [35–39].

After considering all the aforementioned aspects, the processing and characterisation of a new synthetic Si–Ca–P ceramic 3D porous scaffold was achieved from a eutectoid composition 31 wt% TCP - 69 wt% C₂S after heat treatment as regards the nominal composition described in the literature [21].

The mineralogical characterisation showed a biphasic material that was composed of α'-C₂S and Nurse's A Phase. The sharp peaks and low background suggested that the material was highly crystalline with both phases co-existing in equilibrium (Fig. 1). Another critical aspect to create 3D scaffolds by the polymer sponge replica method is particle size. Fig. 2 A shows all the particle size distributions for the different milling times tested herein (from 30 min to 4 h). This was carried out because particle size was directly related to slurry preparation and sintering as some forces increase in line with particle size to produce agglomerates that precipitate, which is a limiting factor in stable slurry production [40]. It is emphasised that the suspension must be sufficiently fluid-like to enter the 3D structure and must have the capacity to remain in the sponge once impregnations have been made. As a result, we obtained a fine ceramic powder with a narrow particle size distribution to cover the polymer walls uniformly and sintered into a dense ceramic material [41]. In parallel to this study, a XRD analysis was performed to assess the crystallinity degree of the ceramic material milled at different times (Fig. 2 B). With increasing milling times, the mechanical energy of the Zr balls also rose, but the sample crystal size became smaller [42]. In our case, at long milling times Zr balls were able to more easily to deform the small crystals making up the material, which resulted in crystallinity loss from 1.5 h, being higher as the milling time period increases. At the end of both studies, the optimal milling time was 2 h, which led to the most homogenous particle size distribution and an average particle size of 32.30 μm in a 90% sample volume.

By the polymer sponge replica method, we coated the polymer sponges with the above ceramic slurry, dried them at room temperature for 1 d and sintered them using optimised heat treatment. In this way, a ceramic 3D scaffold was obtained (displayed in Fig. 3 A, B) with open pores, uniform dimensions and a macroscopy morphology. SEM was used to observe the interconnected porosity and its microstructure, shown in Fig. 4 A. The resultant scaffolds presented an interconnected porous network with an open pores structure that resembled the polyurethane sponge acting as a template. The obtained size pores corresponded to an average size range of 300 μm–600 μm, which agreed with the pore size of the polyurethane template. After chemical etching with HAC (1%) for 60 s, the sample surface with a nominal composition presented a specific topography showing rosettes (Fig. 4 D), which resembled the lamellar structure of the eutectoid composition. These results clearly agree with those previously published by Rubio, et al., who worked with a dense ceramic in 2011 [21].

In order to characterise the sample's chemical bond, ATR-FTIR was run on the scaffold. The silicates and phosphate spectra were characterised by the SiO₄²⁻ and PO₄³⁻ tetrahedral units. Spectra (Fig. 5) showed bands related to the phosphate groups at low wavenumbers of 500–600 cm⁻¹ and between 800 and 1100 cm⁻¹. Bands were also found to be related with the Si–O–Si network (800–1100 cm⁻¹), but were overlapped by the bands corresponding to the PO₄³⁻ groups. The presence of such groups in the ATR-FTIR spectra indicated that it was a Si–P ceramic scaffold.

The mercury porosimetry technique was employed to measure the scaffold's porosity. As seen, the cumulative volume curve (Fig. 6 A)

denoted a high volume intrusion in the structure with a pore size between 65.8 μm and 28.3 μm, followed by a plateau to 1.02 μm, where no intrusion volume was detected. Then a stepped volume intrusion was observed between 1.02 μm and 0.049 μm. The first volume intrusion curve (Fig. 6 A) corresponded to a pore size of about 51.28 μm (Fig. 6 B) and the stepped volume intrusion (Fig. 6 A) corresponded to the pores size range between 667 nm and 55.12 nm (Fig. 6 B). The first volume intrusion curve corresponded to the interparticles spaces filling, whereas the second stepped one corresponded to the intraparticles spaces filling. We were able to create a porous scaffold with a hierarchised structure reaching a tiny nanometric pore size. According to the porosity effect on bone regeneration and bioactivity, authors like Lew, et al. have reported that pores around 100–150 μm enhance cellular adhesion and pre-osteoblasts proliferation [11]. Other authors such as Hadjicharalambous, et al. and Rabadan, et al. have reported that pores > 300 μm improve cell migration, osteoblast proliferation/spreading and new vascular tissue formation through the structure, which improves the supply of nutrients to the cells located inside the porous network by enhancing new bone tissue formation [13,43]. The presence of microporosity may enhance ionic exchange on the scaffold surface that comes into contact with SBF, which improves scaffold bioactivity [44]. Increased pore size is linked to an increase in the volume of empty spaces, which gave poor mechanical properties [39]. However, the obtained scaffolds presented good manipulability. By bearing in mind the data summarised in Table 1, the scaffold would have good osteoconductive and osteoinductive properties given a synergistic combination between macroporosity and microporosity that would result in 95% total open porosity.

Strong *in vitro* bioactivity took place when scaffolds were soaked in SBF (6 h) (Fig. 7 A). This marked bioactivity is related to the chemical composition and the particular microstructure topography of the eutectoid material [12]. The mayor ion exchange between the sample and SBF took place in this lamellar structure. The lamellar microstructure increased the specific surface (0.36 m²/g in the scaffold) and enhanced the ionic exchange because more material came into contact with SBF to allow ionic release than if it were a smooth surface. Other authors, like Padilla et al. [45], and Karamian et al. [46], created a biphasic material by mixing HA with different amounts of 5S5 powder (5% and 20%) and varying amounts of baghdetite (0%–30%), respectively. These biomaterials presented a polycrystalline biphasic microstructure with a granular distribution. The surface was completely covered by HA after soaking for 7 days SBF for Padilla and after 28 days for Karamian. Another biphasic scaffold was created by Lenka Novotna et al. by the *in situ* foaming of a dispersion of diisocyanate, polyol, H₂O and HA which, after heat treatment, transformed into a biphasic calcium phosphate scaffold. They sintered scaffolds at 1050 °C, 1200 °C and 1350 °C. All the scaffolds also presented a granular microstructure. After being soaked for 21 d in SBF, the 1050 °C scaffold showed no HA layer on its surface, and the 1200 °C/1300 °C scaffolds were almost covered by an HA layer [28]. Given these examples, we could state that a proper surface microstructure combined with an appropriate composition may result in a condition used to develop materials with suitable bioactivity.

In light of these results, the bioactivity mechanism is a dissolution/precipitation process. In the first part of the assay, the phase dissolution process was denoted by an increase in the Si ions in SBF and by a slight precipitation process of CHA, which corresponded to a reduction in Ca in SBF (Fig. 9). This behaviour was also supported by the changes in the scaffold surface morphology (Fig. 7 A) compared to the scaffold morphology before soaking in SBF (Fig. 4). We are unaware of the dissolving phase, but it might be the C₂S phase because only the Si and Ca ion concentrations increased. In the second part of the assay, two processes occurred at the same time: Nurse's A phase started to dissolve at the same time as the CHA precipitation process occurred. Nurse's A phase dissolution explained the higher Ca ion concentration, while the CHA precipitation process explained the lowered P ion concentration. The new precipitated layer needed more P and Ca ions than the amount of

ion released from the scaffold. Finally, at the end of the assay, a huge amount of CHA was deposited on the sample surface (Fig. 7 D) and was mechanically unstable. Therefore, CHA dropped from the sample and fell into SBF increasing the Ca ions concentration (from 14 d to 21 d and from 460.32 mg/l to 624.8182 mg/l, respectively) and the P ions concentration (from 14 d to 21 d and from 80.7 mg/l to 81.15 mg/l, respectively). At the end of the test, SBF was slightly cloudy, which reinforces the fact that part of the new precipitated layer had fallen from the scaffold surface.

SBF reached all the scaffold zones due to its interconnected porosity, and ion change took place in all the scaffold areas that came into contact with SBF. This was verified by the presence of a precipitate in both the outside and inside areas. After being analysed by ATR-FTIR, spectra showed bands related to both OH⁻ and CO₃²⁻. This indicates that the CO₃²⁻ groups substituted the PO₄³⁻ groups in the HA crystalline structure (B-type substitution). This was also confirmed by the absence of the 1130 cm⁻¹ peak [29,30]. These results suggest the formation of B-type carbonate hydroxyapatite (CHA) when the sample comes into contact with SBF.

We conclude that a scaffold with an irregular lamellar microstructure composed by two phases of different degradation rates would be a good new approach to develop scaffolds with hierarchical pore distribution and level to serve as a bone tissue engineering guide. Finally, cell studies need to be conducted to assess its biocompatibility.

5. Conclusions

By using the subsystem 7CaOP₂O₅2SiO₂-2CaOSiO₂ in the system C₂S - TCP, a biphasic 3D porous ceramic scaffold with chemical composition 31 wt% TCP-69 wt% C₂S and an irregular lamellar morphology of alternative lamellae of C₂S, Nurse's A phases as well as high interconnected porosity (~ 95%) was created.

The combination of specific physico-chemical factors caused the scaffold's particular *in vitro* behaviour. These results confirmed that our scaffold possesses fast (6 h) and strong bioactivity by showing at the end of the assay a partial material transformation into CHA on both scaffold's areas. This confirms that the 3D porous scaffold obtained herein favours the flow of SBF through the whole porous network to allow a complete ion exchange between SBF and the full sample surface area. The scaffold's bioactivity not only depends on physiological SBF features, but also on the chemical composition, structure and microstructure. These results suggest that scaffolds could be useful for future applications in bone tissue engineering.

References

- [1] R. Agarwal, A.J. Garcia, Biomaterial strategies for engineering implants for enhanced osseointegration and bone repair, *Adv. Drug Deliv. Rev.* 94 (2015) 53–62, <https://doi.org/10.1016/j.addr.2015.03.013>.
- [2] P. Ros-Tarraga, A. Murciano, P. Mazon, S.A. Gehrke, P.N. De Aza, New 3D stratified Si-Ca-P porous scaffolds obtained by sol-gel and polymer replica method: microstructural, mineralogical and chemical characterization, *Ceram. Int.* 43 (8) (2017) 6548–6553, <https://doi.org/10.1016/j.ceramint.2017.02.081>.
- [3] H. Shao, Y. He, J. Fu, D. He, X. Yang, J. Xie, et al., 3D printing magnesium-doped wollastonite/beta-TCP bioceramics scaffolds with high strength and adjustable degradation, *J. Eur. Ceram. Soc.* 36 (6) (2016) 1495–1503, <https://doi.org/10.1016/j.jeurceramsoc.2016.01.010>.
- [4] C. Gao, Y. Deng, P. Feng, Z. Mao, P. Li, B. Yang, et al., Current progress in bioactive ceramic scaffolds for bone repair and regeneration, *Int. J. Mol. Sci.* 15 (3) (2014) 4714–4732, <https://doi.org/10.3390/ijms15034714>.
- [5] V. Karageorgiou, D. Kaplan, Porosity of 3D biomaterial scaffolds and osteogenesis, *Biomaterials* 26 (27) (2005) 5474–5491, <https://doi.org/10.1016/j.biomaterials.2005.02.002>.
- [6] D.W. Hutmacher, Scaffolds in tissue engineering bone and cartilage, *Biomaterials* 21 (24) (2000) 2529–2543, [https://doi.org/10.1016/s0142-9612\(00\)00121-6](https://doi.org/10.1016/s0142-9612(00)00121-6).
- [7] S.M. Naga, H.F. El-Maghraby, E.M. Mahmoud, M.S. Talaat, A.M. Ibrahim, Preparation and characterization of highly porous ceramic scaffolds based on thermally treated fish bone, *Ceram. Int.* 41 (10) (2015) 15010–15016, <https://doi.org/10.1016/j.ceramint.2015.08.057>.
- [8] G.J. Lugo, P. Mazon, P.N. De Aza, Material processing of a new calcium silico-phosphate ceramic, *Ceram. Int.* 42 (1) (2016) 673–680, <https://doi.org/10.1016/j.ceramint.2015.08.164>.
- [9] F.S.L. Bobbert, A.A. Zadpoor, Effects of bone substitute architecture and surface-properties on cell response, angiogenesis, and structure of new bone, *J. Mater. Chem. B* 5 (31) (2017) 6175–6192, <https://doi.org/10.1039/C7TB00741H>.
- [10] C.M. Murphy, M.G. Haugh, F.G. O'Brien, The effect of mean pore size on cell attachment, proliferation and migration in collagen-glycosaminoglycan scaffolds for bone tissue engineering, *Biomaterials* 31 (2010) 461–466, <https://doi.org/10.1016/j.biomaterials.2009.09.063>.
- [11] K.-S. Lew, R. Othman, K. Ishikawa, F.-Y. Yeoh, Macroporous bioceramics: a remarkable material for bone regeneration, *J. Biomater. Appl.* 27 (3) (2012) 345–358, <https://doi.org/10.1177/0885328211406459>.
- [12] H.Y. Niu, D. Lin, W. Tang, Y.F. Ma, B. Duan, Y. Yuan, et al., Surface topography regulates osteogenic differentiation of MSCs via crosstalk between FAK/MAPK and ILK/beta-Catenin pathways in a hierarchically porous environment, *ACS Biomater. Sci. Eng.* 3 (12) (2017) 3161–3175, <https://doi.org/10.1021/acsbomaterials.7b00315>.
- [13] R. Rabadan-Ros, P.A. Velasquez, L. Meseguer-Olmo, P.N. De Aza, Morphological and structural study of a novel porous nurse's ceramic with osteoconductive properties for tissue engineering, *Materials* 9 (6) (2016), <https://doi.org/10.3390/ma9060474>.
- [14] F. Scalera, F. Gervaso, K.P. Sanosh, A. Sannino, A. Licciulli, Influence of the calcination temperature on morphological and mechanical properties of highly porous hydroxyapatite scaffolds, *Ceram. Int.* 39 (5) (2013) 4839–4846, <https://doi.org/10.1016/j.ceramint.2012.11.076>.
- [15] N. Thadavirul, P. Pavasant, P. Supaphol, Development of polycaprolactone porous scaffolds by combining solvent casting, particulate leaching, and polymer leaching techniques for bone tissue engineering, *J. Biomed. Mater. Res. A* 102 (10) (2014) 3379–3392, <https://doi.org/10.1002/jbm.a.35010>.
- [16] M.Z. Moghadam, S. Hassanajili, F. Esmailzadeh, M. Ayatollahi, M. Ahmadi, Formation of porous HPCL/LPCL/HA scaffolds with supercritical CO₂ gas foaming method, *J. Mech. Behav. Biomed. Mater.* 69 (2017) 115–127, <https://doi.org/10.1016/j.jmbbm.2016.12.014>.
- [17] A. Kordjamshidi, S. Saber-Samandari, M.G. Nejad, A. Khandan, Preparation of novel porous calcium silicate scaffold loaded by celecoxib drug using freeze drying technique: fabrication, characterization and simulation, *Ceram. Int.* (2019), <https://doi.org/10.1016/j.ceramint.2019.04.113>.
- [18] A. Salerno, M. Fernandez-Gutierrez, J.S. Roman del Barrio, C. Domingo, Bio-safe fabrication of PLA scaffolds for bone tissue engineering by combining phase separation, porogen leaching and scCO₂ drying, *J. Supercrit. Fluids* 97 (2015) 238–246, <https://doi.org/10.1016/j.supflu.2014.10.029>.
- [19] G. Jin, R. He, B. Sha, W. Li, H. Qing, R. Teng, et al., Electrospun three-dimensional aligned nanofibrous scaffolds for tissue engineering, *Mater. Sci. Eng. C-Mater. Biol. Appl.* 92 (2018) 995–1005, <https://doi.org/10.1016/j.msec.2018.06.065>.
- [20] E. De Giglio, M.A. Bonifacio, A.M. Ferreira, S. Cometa, Z.Y. Ti, A. Stanzione, et al., Multi-compartment scaffold fabricated via 3D-printing as *in vitro* co-culture osteogenic model, *Sci. Rep.* 8 (2018), <https://doi.org/10.1038/s41598-018-33472-1>.
- [21] V. Rubio, M.A. de la Casa-Lillo, S. De Aza, P.N. De Aza, The system Ca₃(PO₄)₂-Ca₂SiO₄: the sub-system Ca₂SiO₄-7CaOP₂O₅2SiO₂, *J. Am. Ceram. Soc.* 94 (12) (2011) 4459–4462, <https://doi.org/10.1111/j.1551-2916.2011.04716x>.
- [22] Hassna Rehman Ramay, Miqin Zhang, Preparation of porous hydroxyapatite scaffolds by combination of the gel-casting and polymer sponge methods, *Biomaterials* 29 (2003) 3293–3302, [https://doi.org/10.1016/S0142-9612\(03\)00171-6](https://doi.org/10.1016/S0142-9612(03)00171-6).
- [23] Mohd Al Amin Muhamad Nor, Lee Chain Hong, Zainal Arifin Ahmad, Hazizan Md Akil, Preparation and characterization of ceramic foam produced via polymeric foam replication method, *J. Mater. Process. Technol.* (207) (2008) 235–239, <https://doi.org/10.1016/j.jmatprotec.2007.12.099>.
- [24] T. Kokubo, H. Takadama, How useful is SBF in predicting *in vivo* bone bioactivity? *Biomaterials* 27 (15) (2006) 2907–2915, <https://doi.org/10.1016/j.biomaterials.2006.01.017>.
- [25] V. Rubio, P. Mazon, M.A. de la Casa-Lillo, P.N. De Aza, Preparation, characterization and *in vitro* behavior of a new eutectoid bioceramic, *J. Eur. Ceram. Soc.* 35 (1) (2015) 317–328, <https://doi.org/10.1016/j.jeurceramsoc.2014.08.039>.
- [26] H. Aguiar, J. Serra, P. Gonzalez, B. Leon, Structural study of sol-gel silicate glasses by IR and Raman spectroscopies, *J. Non-Cryst. Solids* 355 (8) (2009) 475–480, <https://doi.org/10.1016/j.jnoncrysol.2009.01.010>.
- [27] F. Bairo, M. Ferraris, O. Bretcanu, E. Verne, C. Vitale-Brovarone, Optimization of composition, structure and mechanical strength of bioactive 3-D glass-ceramic scaffolds for bone substitution, *J. Biomater. Appl.* 27 (7) (2013) 872–890, <https://doi.org/10.1177/0885328211429193>.
- [28] L. Novotna, L. Kucera, A. Hampl, D. Drdlik, J. Cihlar Jr., J. Cihlar, Biphasic calcium phosphate scaffolds with controlled pore size distribution prepared by *in-situ* foaming, *Mater. Sci. Eng. C-Mater. Biol. Appl.* 95 (2019) 363–370, <https://doi.org/10.1016/j.msec.2018.03.022>.
- [29] N.S. Resende, M. Nele, V.M.M. Salim, Effects of anion substitution on the acid properties of hydroxyapatite, *Thermochim. Acta* 451 (1–2) (2006) 16–21, <https://doi.org/10.1016/j.tca.2006.08.012>.
- [30] I.M. Martinez, L. Meseguer-Olmo, A. Bernabeu-Esclapez, P.A. Velasquez, P.N. De Aza, *In vitro* behavior of alpha-tricalcium phosphate doped with dicalcium silicate in the system Ca₂SiO₄-Ca-3(PO₄)₂, *Mater. Char.* 63 (2012) 47–55, <https://doi.org/10.1016/j.matchar.2011.10.013>.
- [31] L. Berzina-Cimdina, N. Borodajenko, Research of Calcium Phosphates Using Fourier Transform Infrared Spectroscopy, *Infrared Spectroscopy. Mater. Sci. Eng. Technol.* (2012) 123–148, <https://doi.org/10.5772/36942>.
- [32] A. Kolk, J. Handschel, W. Drescher, D. Rothamel, F. Kloss, M. Blessmann, et al., Current trends and future perspectives of bone substitute materials - from space holders to innovative biomaterials, *J. Cranio-Maxillofacial Surg.* 40 (8) (2012)

- 706–718, <https://doi.org/10.1016/j.jcms.2012.01.002>.
- [33] S. Taherkhani, F. Moztafzadeh, Influence of strontium on the structure and biological properties of sol-gel-derived mesoporous bioactive glass (MBG) powder, *J. Sol. Gel Sci. Technol.* 78 (3) (2016) 539–549, <https://doi.org/10.1007/s10971-016-3995-2>.
- [34] I.H. Garcia-Paez, R.G. Carrodeguas, A.H. De Aza, C. Baudin, P. Pena, Effect of Mg and Si co-substitution on microstructure and strength of tricalcium phosphate ceramics, *J. Mech. Behav. Biomed. Mater.* 30 (2014) 1–15, <https://doi.org/10.1016/j.jmbbm.2013.10.011>.
- [35] R. Rabadan-Ros, P. Velásquez, L. Meseguer-Olmo, P.N. De Aza, Morphological and structural study of a novel porous Nurse's A ceramic with osteoconductive properties for tissue engineering, *Materials* 9 (6) (2016) 474 <https://doi.org/10.3390/ma9060474>.
- [36] A. Parrilla-Almansa, N. García-Carrillo, P. Ros-Tárraga, C.M. Martínez, F. Martínez-Martínez, L. Meseguer-Olmo, P.N. de Aza, Demineralized bone matrix coating Si-Ca-P ceramic does not improve the osseointegration of the, *Scaffold Mater* 11 (2018) 1580 <https://doi.org/10.3390/ma11091580>.
- [37] B. Otsuki, M. Takemoto, S. Fujibayashi, M. Neo, T. Kokubo, T. Nakamura, Pore throat size and connectivity determine bone and tissue ingrowth into porous implants: three-dimensional micro-CT based structural analyses of porous bioactive titanium implants, *Biomaterials* 27 (35) (2006) 5892–5900, <https://doi.org/10.1016/j.biomaterials.2006.08.013>.
- [38] P.N. De Aza, M.A. Rodríguez, S.A. Gehrke, J.E. Maté-Sánchez de Val, J.L. Calvo-Guirado, A Si- α -TCP scaffold for biomedical applications: an experimental study using the rabbit tibia model, *Appl. Sci.-basel.* 7 (2017) 706 <https://doi.org/10.3390/app7070706>.
- [39] I. Bruzuskaitė I, D. Bironaitė, E. Bagdonas, E. Bernotienė, Scaffolds and cells for tissue regeneration: different scaffold pore sizes-different cell effects, *Cytotechnology* 68 (2016) 355–369.
- [40] E. Cunningham, N. Dunne, G. Walker, F. Buchanan, High-solid-content hydroxyapatite slurry for the production of bone substitute scaffolds, *Proc. Inst. Mech. Eng. H J. Eng. Med.* 223 (H6) (2009) 727–737, <https://doi.org/10.1243/09544119jeim564>.
- [41] L. Montanaro, Y. Jorand, G. Fantozzi, A. Negro, Ceramic foams by powder processing, *J. Eur. Ceram. Soc.* 18 (9) (1998) 1339–1350, [https://doi.org/10.1016/S0955-2219\(98\)00063-6](https://doi.org/10.1016/S0955-2219(98)00063-6).
- [42] C. Ruiz-Aguilar, U. Olivares-Pinto, E.A. Aguilar-Reyes, R. Lopez-Juarez, I. Alfonso, Characterization of beta-tricalcium phosphate powders synthesized by sol-gel and mechanochemical synthesis, *Bol. Soc. Espanola Ceram. Vidr.* 57 (5) (2018) 213–220, <https://doi.org/10.1016/j.bsevcv.2018.04.004>.
- [43] C. Hadjicharalambous, O. Prymak, K. Loza, A. Buyakov, S. Kulkov, M. Chatzinikolaïdou, Effect of porosity of alumina and zirconia ceramics toward pre-osteoblast response, *Front. Bioeng. Biotechnol.* 3 (2015), <https://doi.org/10.3389/fbioe.2015.00175> 175–175.
- [44] X. Li, C.A. van Blitterswijk, Q. Feng, F. Cui, F. Watari, *The Effect of Calcium Phosphate Microstructure on Bone-Related Cells in Vitro*, *Biomaterials* (2008).
- [45] S. Padilla, J. Roman, S. Sanchez-Salcedo, M. Vallet-Regi, Hydroxyapatite/SiO₂-CaO-P₂O₅ glass materials: in vitro bioactivity and biocompatibility, *Acta Biomater.* 2 (3) (2006) 331–342, <https://doi.org/10.1016/j.actbio.2006.01.006>.
- [46] E. Karamian, A. Nasehi, S. Saber-Samandari, A. Khandan, Fabrication of hydroxyapatite-baghdadite nanocomposite scaffolds coated by PCL/Bioglass with polyurethane polymeric sponge technique, *Nanomed. J.* 4 (3) (2017) 177–183, <https://doi.org/10.22038/nmj.2017.8959>.

Artículo 2

Rightslink® by Copyright Clearance Center

<https://s100.copyright.com/AppDispatchServlet#formTop>



RightsLink®



Home



Help



Email Support



Sign in



Create Account



Easy manufacturing of 3D ceramic scaffolds by the foam replica technique combined with sol-gel or ceramic slurry

Author:

Carlos Navalón, Patricia Ros-Tárraga, Angel Murciano, Pablo Velasquez, Patricia Mazón, Piedad N. De Aza

Publication: Ceramics International

Publisher: Elsevier

Date: 15 October 2019

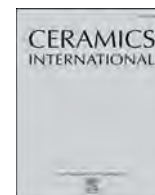
© 2019 Elsevier Ltd and Techna Group S.r.l. All rights reserved.

Please note that, as the author of this Elsevier article, you retain the right to include it in a thesis or dissertation, provided it is not published commercially. Permission is not required, but please ensure that you reference the journal as the original source. For more information on this and on your other retained rights, please visit: <https://www.elsevier.com/about/our-business/policies/copyright#Author-rights>

BACK

CLOSE WINDOW

© 2020 Copyright - All Rights Reserved | [Copyright Clearance Center, Inc.](#) | [Privacy statement](#) | [Terms and Conditions](#)
Comments? We would like to hear from you. E-mail us at customercare@copyright.com



Easy manufacturing of 3D ceramic scaffolds by the foam replica technique combined with sol-gel or ceramic slurry

Carlos Navalón^a, Patricia Ros-Tárraga^b, Angel Murciano^c, Pablo Velasquez^a, Patricia Mazón^c, Piedad N. De Aza^{a,*}

^a Instituto de Bioingeniería, Universidad Miguel Hernández, Avda. Ferrocarril s/n, 03202, Elche, Alicante, Spain

^b Grupo de Investigación en Regeneración y Reparación de Tejidos. UCAM-Universidad Católica San Antonio de Murcia, 30107, Guadalupe, Murcia, Spain

^c Departamento de Materiales, Óptica y Tecnología Electrónica, Universidad Miguel Hernández, Avda. Universidad s/n, 03202, Elche, Alicante, Spain

ARTICLE INFO

Keywords:

Sol-gel processes
Suspensions
Microstructure-final
Silicate
Biomedical applications

ABSTRACT

A material, whose composition was based on the SiO₂-CaO-P₂O₅ system, was used to prepare 3D porous ceramic scaffolds made by the foam replication technique linking the sol-gel route or ceramic slurry in barbotine suspension processes. With an appropriate heat treatment, it was possible to obtain a 3D-scaffold containing two crystalline phases or more, and a controlled nano-to microscale microstructure. The obtained scaffolds presented an interconnected and well-defined porous structure. Its pore size was 0.060–600 μm. It had a rough pore wall that could potentially benefit ingrowth and cell adhesion.

In terms of hydroxycarbonate apatite formation in simulated body fluid (SBF), the 3D scaffolds' bioactivity was confirmed after 3 and 14 days of immersion in SBF. This clearly confirms that these new scaffolds are suitable for bone regeneration applications. Processing technology allows 3D scaffolds to be adapted with particular microstructures to increase/decrease their *in vitro* behavior.

1. Introduction

In the last decade, much interest has been shown in dense ceramic materials based on monolithic [1,2] and biphasic Si-Ca-P (SCP) [3,4], and even in three phasic materials [5], to develop new implant materials. Porous SCP-based scaffolds for bone tissue engineering have recently attracted increasingly more attention thanks to their competency and bioactivity to act as a 3D template for bone growth [6,7]. Of all the methods available to produce these scaffolds, the foam replication technique allows highly interconnected (trabecular) pore structures with a controllable pore size to be obtained with a sacrificial polyurethane foam template [8,9].

Bioactive 3D scaffolds synthesized by the sol-gel route provide particles with a large surface area and superficial porosity [8,10], while ceramic slurry in a barbotine suspension generates scaffolds with suitable pore size and controlled porosity to imitate bone structure by enabling the material to act as a framework for new bone tissue deposition [4,11,12].

Most scaffolds developed today are polycrystalline biphasic scaffolds with a granular distribution of phases, like silicocarnotite/Nurse's A [11]. HA/TCP [13], or diopside/Calcium-phosphate [14]. The

dissolution of one phase or several leads to loss of mechanical properties as large pores are generated. It is well-known that in dense ceramics with structures developed by the slow cooling down of a composition belonging to an invariant point, a polycrystalline structure with an irregular lamellar distribution of phases is obtained [15,16]. The dissolution of the greater solubility phase allows that of lower solubility to remain by transforming a ceramic dense into a porous one given the mechanical support during bone neoformation [17,18]. Our intention was to develop structures with interconnected porosity and a eutectoid composition in the SiO₂-CaO-P₂O₅ system.

The crystallization stages of the eutectoid 2CaOSiO₂-3CaOP₂O₅ ceramic were herein investigated to develop biodegradable and bioactive scaffolds with structural and microstructural optimized properties.

The 3D scaffolds' bioactivity was investigated in terms of hydroxycarbonate apatite (HCA) formation in SBF as an initial indicator of such bioactivity. The effect of both phase composition and the microstructure on the 3D scaffold ceramics' *in vitro* behavior in SBF was studied.

* Corresponding author. Instituto de Bioingeniería Universidad Miguel Hernandez, 03202, Elche, Alicante, Spain.

E-mail addresses: carlos.navalon@goumh.umh.es (C. Navalón), pros@ucam.edu (P. Ros-Tárraga), amurciano@umh.es (A. Murciano), pavelasquez@umh.es (P. Velasquez), pmazon@umh.es (P. Mazón), piedad@umh.es (P.N. De Aza).

<https://doi.org/10.1016/j.ceramint.2019.06.048>

Received 4 February 2019; Received in revised form 20 May 2019; Accepted 5 June 2019

Available online 06 June 2019

0272-8842/ © 2019 Elsevier Ltd and Techna Group S.r.l. All rights reserved.

2. Materials and methods

In order to obtain 3D scaffolds with the nominal composition 24.3 wt% SiO₂-61.65 wt%CaO-14.18 wt% P₂O₅ that belongs to the invariant eutectoid point, two processing routes were used.

- (i) A water-based sol prepared according to Ros-Tárraga et al. [8] was used. In a classic synthesis procedure: 8.93 mL of TEOS (Aldrich-98%, St. Louis MO, USA), 3.39 mL of TEP (Aldrich-98%, St. Louis MO, USA), 5 mL of ethanol 97° and 10 mL of HCl drop by drop to avoid TEOS gelation were added to 20 mL of distilled water with constant stirring at room temperature for 30 min for complete homogenization. To this solution, 11 g of CaCO₃ (Sigma, > 99 wt%, St. Louis, MO, USA) were added. A final transparent solution with a pH between 2 and 3 was obtained.
- (ii) Ceramic slurry in a barbotine suspension was prepared with 60% solid contents of SiO₂ > 99.7 wt% (Strem Chemicals Inc., Newburyport, MA, USA), CaCO₃ > 99.0 wt% (Sigma St. Louis MO, USA) and CaHPO₄ (Panreac, Castellar del Valles, Spain) previously synthesized in our laboratory [3] whose particle size was 13.76 μm (Mastersizer, Malvern, PA, USA) in water media. We employed 2 wt % of defloculant (Dolapix CE-64—Zschimmer Schwartz, Germany) and 8 wt % of binder (Optapix PAF-35—Zschimmer Schwartz, Germany) to obtain a powder/water ratio of 60:40.

Polyurethane (PU-Eurofoam, Germany) foams with 30 ppi (1 cm diameter, 0.7 cm height) were utilized as sacrificial nonconductive templates to manufacture the scaffolds.

Normally when using sol-solutions or barbotine suspension, several impregnations are necessary before burning out the PU in order to create a thick enough structure to hold the scaffold's weight. In our case, 25 PU immersions were performed in the sol-solution and 3 immersions in the barbotine suspension. Slurry in excess was squeezed out. Then the PU foam was blown using compressed air to ensure that the coating on the PU foam surface was uniform, and that no closing faced the next dives. Finally, the PU covered with the solutions was dried until constant weight was measured (10 min at 160–180 °C.).

The PU with the sol-solution was sintered in a muffle furnace (Nabertherm, Lilienthal/Bremen, Germany) at 950 °C at a slow heating rate of 0.5°/min. in order to evaporate the remaining solvents and to burn out the PU, which was left at 950 °C for 8 h to consolidate the 3D scaffold. Next the power was switched off to let the scaffolds cool down inside the furnace. The diameter and length of the final scaffolds was 0.8 cm and 0.5 cm, respectively. The PU with the barbotine suspension was sintered in a high-temperature electrical furnace (Enthec-Jumo Imago 500 model, Angelholm, Sweden) in two different sintering stages: 1550 °C/3 h at a heating rate of 3 °C/min, a cooling rate of 1 °C/min until 512 °C/24 h, followed by a drop in room temperature within 24 h. The final scaffolds had a diameter of 0.9 cm and a length of 0.6 cm.

In order to establish the crystalline phases precipitated in the scaffolds' heat treatment, an X-Ray Diffraction (XRD) analysis was run to qualitatively identify them. Next scaffolds were ground to less than 60 μm, and XRD patterns were carried out by an X-Ray Bruker-AXS D8 Advance automated diffractometer with CuKα1.2 radiation (1.541874 Å) and a secondary curved graphite monochromator. Data were acquired by the Bragg-Brentano (Theta/2Theta) vertical geometry (in the flat reflection mode) from 10° to 60° (2Theta) and in 0.02° steps by counting 20s/step. The X-ray tube ran at both 40 kV and 30 mA. Phases were identified by the Power Diffraction Match! 3 version 33.6.2.121 software and the database provided by the Crystallography Open Database (COD).

An attenuated total reflectance (ATR) Fourier Transform Infrared Spectrometry (FTIR) spectrometer IF66s, Bruker was used to obtain the chemical composition of the scaffolds. A potassium bromide (KBr) tablet was used with 1 mg of KBr for every 150 mg of milled scaffold to be

pressed at 10000 tons. Data were acquired between 4000 and 500 cm⁻¹ at 20 °C and a 300-scan resolution.

The 3D scaffolds' microstructure was characterized by Scanning Electron Microscopy (SEM-EDX, SEM-Hitachi S-3500 N) equipped with an Energy-Dispersive X-Ray Spectroscopy (INCA system, Oxford Instruments Analytical, UK), by covering samples with palladium. In order to investigate the effect of the process parameters on the final microstructure, the scaffolds' ultrastructure was carried out in a Field Emission SEM (FESEM Merlin™ VP compat, Car Zeiss Microscopy S.L. Oberkochen, Germany).

Information on the scaffolds' pore size distribution and on macro- and micro-porosities (%) was obtained by mercury porosimetry with Poremaster-60 GT (Quantachrome Instruments, Boyton Beach, FL, USA) within the 0.200 PSIA-59498.39 PSIA pressure range corresponding to a range of pore diameters from 300 μm to 0.0035 μm. Four samples were studied for each scaffold (~0.4816 g). If a difference > 5% in the porosity values was found, one more sample was analyzed.

To comprehensively investigate both the developed scaffolds' efficacy in order to release bioactive ions to their microenvironments, and their capability to produce CHA, the scaffolds were soaked in SBF, which was prepared according to the protocol of Kokubo et al. and has similar chemical composition and pH to human blood plasma [19]. These bioactivity tests were run inside an incubator in normal air at 70 rpm and 37 °C. Three immersion times were tested (3, 7 and 14 days). No SBF was replaced throughout the incubation period. Fourier Transform Infrared Spectroscopy (FTIR) (Nicolet 6700, Thermo Scientific Germany) was used to assess CHA formation using KBr pellets, 32 scans and a resolution of 4 cm⁻¹, which were repeated within the 4000–500 cm⁻¹ wavenumber range. The above-mentioned SEM was performed to see if any changes in scaffolds took place with time. SBF was removed after some immersion periods, and the calcium, silicon and phosphorus ions were established in the removed SBF by means of inductively coupled plasma optical emission spectrometry (ICP-OES PerkinElmer Optima 2000).

3. Results

Diffractograms showed that the crystalline phases were associated with the SCP-based materials. The scaffold obtained from ceramic slurry in the barbotine suspension processes, referred to henceforth as S-BS, gave a mixture of crystalline calcium silicophosphate (Ca₇P₂Si₂O₁₄) and crystalline α_H-dicalcium silicate (Ca₂SiO₄) (Fig. 1A). The scaffold obtained from a sol-gel route, referred to henceforth as S-SG, was composed of a mixture of silicon oxide (SiO₂) in the polymorphs form of trydimite and cymballite, tricalcium phosphate (Ca₃P₂O₈), pyrophosphate (Ca₂P₂O₇) and α_H-dicalcium (Ca₂SiO₄) (Fig. 1 B).

The ATR-FTIR spectra of both scaffolds are shown in Fig. 2 and Table 1. The three main vibrational modes of the Si–O–Si groups were observed in the region lying between 700 and 1300 cm⁻¹. The Si–O–Si vibration group was noted between 760 and 975 cm⁻¹, where oxygen moved at right angles to both the Si–O–Si planes and Si–Si lines. The last bands that went from 1000 to 1300 cm⁻¹ were related to the asymmetrical stretching Si–O–Si mode, where the bridging oxygen atoms moved in the opposite direction to their Si neighbors, and ran approximately in parallel to the Si–Si lines. However, the existence of modifier elements in the network as alkali-earth elements, like calcium in our scaffolds [20,21], modified these structures, with two new bands appearing at 848 cm⁻¹ (Si–O–2NBO) and between 890 and 975 cm⁻¹ (Si–O–NBO) given the increasing number of non bridging oxygen. These bands can shift toward lower wavenumbers and can broaden [22,23].

The presence of PO₄³⁻ groups in the scaffolds was demonstrated in three main regions: (i) two well resolved peaks at 563/566 cm⁻¹ and 586/583 cm⁻¹ assigned to the asymmetric bending modes; (ii) several peaks between 900 and 970 cm⁻¹ corresponding to the symmetric stretching vibration mode; (iii) another group of several peaks between

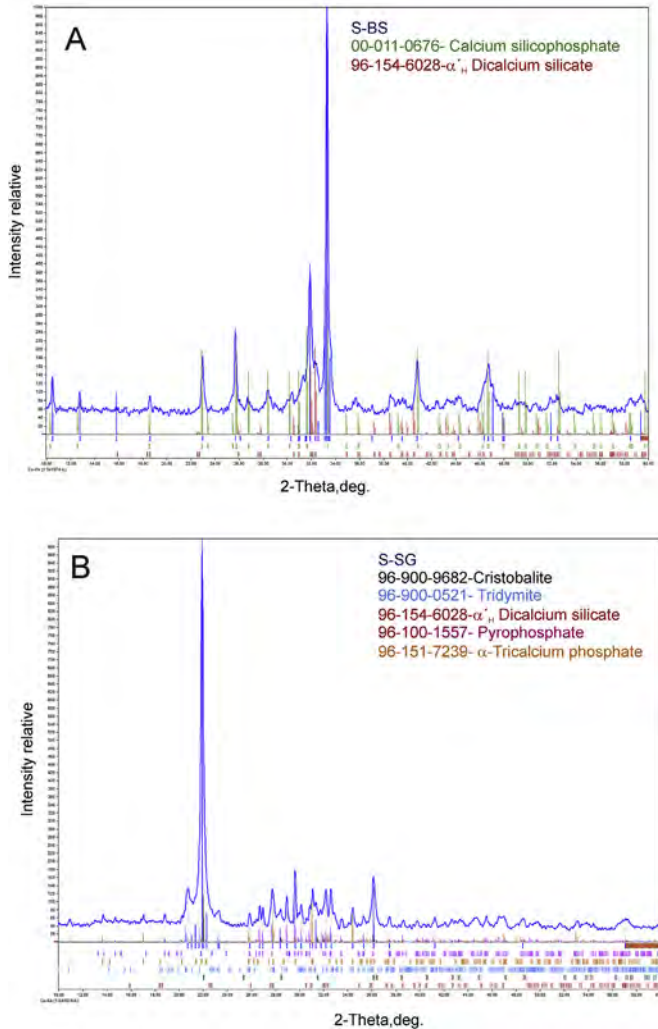


Fig. 1. XRD of (A) powder scaffolds S-BS and (B) S-SG.

1080 and 1100 cm^{-1} associated with the asymmetric stretching vibration mode [18]. The lower intensity, broadening and shifting of these peaks were found in those samples with either poor stoichiometry or less crystallinity.

The SEM examination (Figs. 3–5) revealed a highly porous structure for both prepared scaffolds, with pore interconnectivity regardless of the processing method. The SEM observation revealed that the S-SG material comprised typical big spherical pores (porosity $\sim 95\%$ and pore size $\sim 300\text{--}600\ \mu\text{m}$, Table 2) and small interconnecting oval pores, as Fig. 3 depicts. The large spherical pore size was roughly $600\ \mu\text{m}$. Many small pores were distributed around the big spherical pore walls, and generally fell within the $1\text{--}6\ \mu\text{m}$ size range (Fig. 3B). These pores were highly interconnected, as confirmed by mercury porosimetry, and as Fig. 6 and Table 2 show. Many small pores within the size range of several μm , or even smaller, were found. These walls could have been formed by adding the surfactant (Fig. 3C).

S-BS (Fig. 4A) also showed a highly porous (porosity $\sim 94.8\%$, pore size $\sim 300\text{--}600\ \mu\text{m}$, Table 2) structure with some broken struts and a triangular hole that the PU left when it was eliminated by heat treatment. Fig. 4B shows the wall microstructure features, which consisted of the homogeneous presence of swallowing and microcracks, probably due to heat treatment. A close up (Fig. 4C) reveals a dendritic feature of nanometric size, together with microcracks.

The typical FESEM microstructure of the chemical etched S-BS scaffold is shown in Fig. 5. The dendritic feature presents a lamellar morphology composed of lamellae with different etching rates. The

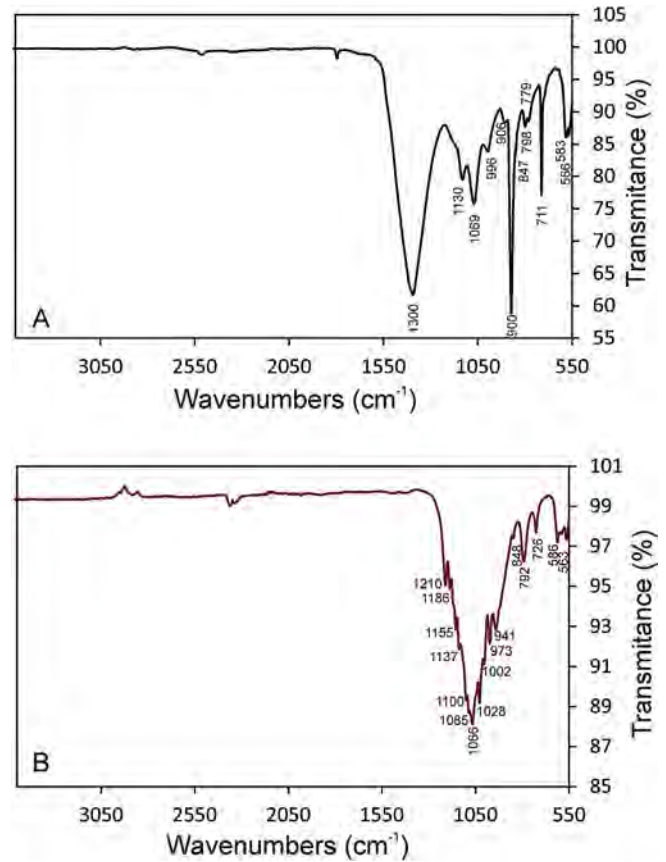


Fig. 2. ATR-FTIR spectra of (A) scaffolds S-BS and (B) S-SG.

Table 1

Assignments of the ATR-FTIR vibrational modes of the synthesized 3D scaffolds [14–18].

Wavenumbers (cm^{-1})	Vibrations
1200	P–O–P asymmetric stretching
1000–1300	Si–O–Si asymmetric stretching
1080–1100	PO_4^{3-} asymmetric stretching
900–980	Si–OH symmetric stretching
900–970	PO_4^{3-} symmetric stretching
890–975	Si–O–NBO stretching
760–850	Si–O–Si bending
848	Si–O–2NBO stretching
720	P–O–P stretching
500–600	PO_4^{3-} asymmetric bending

scaffold wall was made up of very thin lamellae that constituted dicalcium silicate and calcium silicophosphate (Fig. 1A). The EDS analysis confirmed that the phase eliminated by chemical etching was dicalcium silicate, while that observed actually corresponded to phosphorous deficient calcium silicophosphate (Fig. 5B). This was checked by the comparison made with the previously reported calcium silicophosphate monophasic material (Fig. 5C) [2].

Mercury porosimetry gave us information about two types of spaces: interparticle spaces related to the empty spaces between particles; intraparticle spaces related to the spaces of the particles themselves (commonly identified as pores). The scaffold obtained by the sol-gel route showed constant mercury intrusion in the pores within practically the whole range of the porosimetry equipment ($300\ \mu\text{m}$ and $0.0035\ \mu\text{m}$) (Fig. 6A). So the range to distinguish between the intra- and interparticle spaces was not clear. The intraparticle pores range became more evident for the scaffold obtained from a barbotine suspension, in which an intense peak at $51.3\ \mu\text{m}$ was clearly visible and corresponded

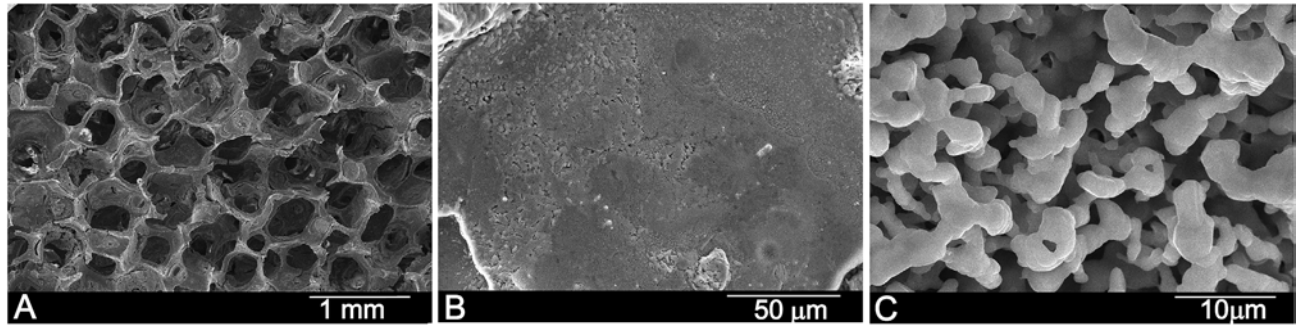


Fig. 3. SEM image of the S-SG scaffold at different magnifications.

to the mercury intrusion in the interparticle spaces. Nevertheless, the division that formed between the intra- and interparticle spaces was not always that ostensible. This interpretation helps to clarify the kind of information that can be drawn from the pore size distribution curves, and highlighted the importance of always specifying the size range of the measured pores. In this case, the interparticle spaces were between the upper limit detection and $1\ \mu\text{m}$, while the intraparticle spaces were between $1\ \mu\text{m}$ and the lower limit detection. It should be indicated that the mercury porosimetry technique is particularly apt for examining intraparticle pores, but not for measuring big spaces ($> 300\ \mu\text{m}$).

In Fig. 6B, S-SG presents a slope in the pores between $300\ \mu\text{m}$ and $4.2\ \mu\text{m}$, followed by another small slope between 4.2 and $0.18\ \mu\text{m}$, after which no intrusion was detected. Scaffold S-B shows a high concentration of pore size. A considerable mercury intrusion close to the vertical slope can be seen between 70 and $38\ \mu\text{m}$, followed by a plateau where no mercury intrusion is detected until $1\ \mu\text{m}$. Afterward, there are small mercury intrusions, followed by small plateaus until $0.052\ \mu\text{m}$.

Table 2 summarizes these results. The analysis of Table 2 indicated that the highest porosity (48.9%) went to S-SG. Nevertheless, about 39.66% of this porosity corresponded to submicron pore entrances. However, S-B exhibited much smaller porosity (12.83%). According to the obtained macroporosity, both scaffolds were seen to have a similar total porosity (around 95%).

Figs. 7 and 8 present the surfaces of both S-SG and S-B after immersion in the SBF solution for 3, 7 and 14 days, respectively. These images clearly show differences in these surfaces' morphologies. S-SG was mineral precipitates-free and continued to be almost intact up to 7 days of SBF immersion (Fig. 7). On day 14, the precipitate covering the material was spherical-shaped and its average diameter was $30\ \mu\text{m}$, which joined together to form a compact continuous layer on the surface. The 3D morphology remained after 14 days of immersion, despite the mineral precipitate layer. The larger pores did not close, which indicates that the material can be *a priori* colonized by cells *in vivo*. The higher-magnification SEM image revealed that the agglomerate comprised many minute worm-like crystals whose crystallite size was approximately $350\text{--}450\ \text{nm}$ long and with a diameter of $75\text{--}100\ \text{nm}$. Some microcracks were observed on the scaffold, which were caused by the

soaked scaffolds shrinking in air, and suggests a thick deposition layer forming. The EDS analysis showed that the mineral precipitates consisted mainly in Ca and P, with the slight presence of Si elements.

S-B behaved similarly to S-SG, but slightly differently. Scaffold S-B (Fig. 8) seemed more reactive because the scaffold's surface morphology changed after 3 days of immersion given the presence of a precipitated mineral. On day 3 of immersion, the scaffold surface was covered by cauliflower particles with an average size of $2\text{--}3\ \mu\text{m}$.

On day 7 of immersion, the precipitate progressively grew to form a continuous compact layer on the surface and, consequently, the original scaffold morphology completely changed (Figs. 4 and 5). This morphology did not further change with soaking time but, instead, particles enlarged with longer immersion periods and lost their cauliflower-like morphology. Finally, their average diameter was $\sim 5\ \mu\text{m}$ after a 14-day immersion and they joined as a bigger dense layer. In the same way as with S-SG, the surface cracked due to the scaffold drying. A cross-section of a strut was seen on day 14, which revealed that all the scaffolds had been transformed into a compact Ca–P layer, and left a hollow space that PU occupied when the scaffold was made. Despite the thickness of the precipitated Ca–P layer, it was not enough to close the scaffold's macroporosity and it maintained its 3D structure, but pores were somewhat smaller than the original ones due to the layer of precipitate.

This new layer of precipitate was determined as being hydroxyapatite (HA)-like by the SEM-EDS microanalysis. The Ca/P ratio of the HA-like layer was, on average, ~ 2.8 for S-SG and ~ 2.4 for S-B. In both cases, the ratio was higher than that in the HA stoichiometrics. This fact suggests that carbonate-apatite formed on the surface of both scaffolds.

The changes in the concentrations of the calcium, phosphorous and silicon elements and the ions of SBF measured at different soaking times are shown in Fig. 9. Both scaffolds had increased Si, Ca and P concentrations in the SBF at the beginning of the reaction, released Ca and P at the end of the assay, and only the Si ion increased throughout the experiment. Both scaffolds behaved similarly, but at different times and with varying amounts.

In relation to S-B, the Si, Ca and P ion dissolutions from the

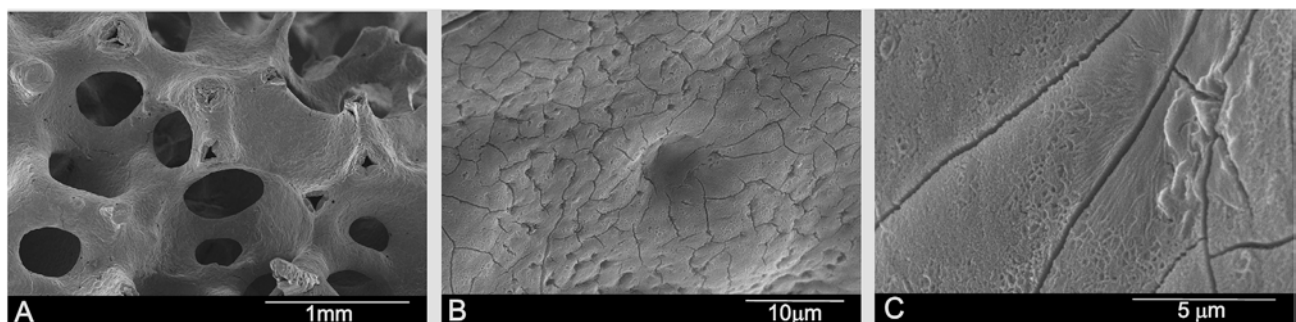


Fig. 4. SEM image of the S-B scaffold at different magnification level.

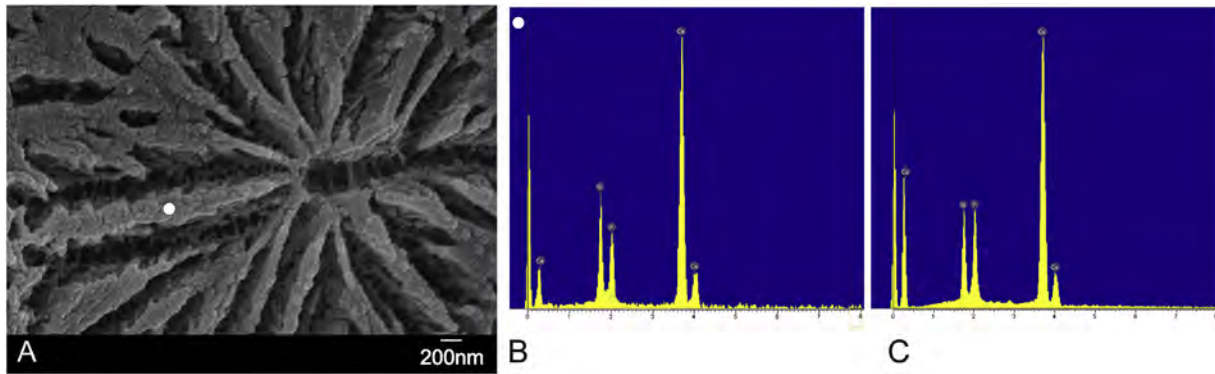


Fig. 5. (A) FESEM image of the chemical etched (Using 1 vol% acetic acid for 4 s) surface of the S-BS scaffold, (B) the EDS microanalysis from the lamella in Fig. 5A and (C) the EDS microanalysis of a calcium silicophosphate material for comparative purposes [2].

Table 2
Physical characteristics of both scaffolds.

(part I)					
Materials	Intruded Volume (cc/g)	Mode of Intraparticle Pores (μm)	Total Porosity (%) ^a	Intraparticle Porosity (%) ^b	Interparticle Porosity (%) ^b
S-BS	0.610	0.76-0.0039	12.83	4.07	8.76
S-SG	0.410	0.6-0.058	48.9	9.24	39.66

^a corresponding to 1 μm < pores < 300 μm; ^b corresponding to pores < 1 μm.

(part II)				
Materials	Pore size (μm)	Scaffold Porosity (%)	Apparent Density (gr/cc)	Surface Area (m ² /g)
S-BS	300–600	94.8	2.59	0.36
S-SG	300–500	95	1.19	1.19

material helped increase the concentration of these ions in SBF until day 7. Element ions P and Ca were removed from SBF on day 14 because of the massive formation of the HA-like phase on the scaffold's surface. The new HA-like precipitated layer was thin (day 7), and even allowed the dissolution of the material and the contribution of new ions to the medium. With time (day 14), the new layer became thicker and, thus, it did not allow the dissolution of the material. Indeed the diffusion processes of the ions across the new HA-like phase to the medium began to become difficult. Thus the only decrease to take places was in the ions as they were consumed to form the new HA-like phase that precipitated on the scaffold.

In relation to S-SG, all the ions in SBF increased until day 3, and this continued (within the equipment error limits) on day 7. This implies a dissolution of the scaffold. On day 14 an evident descent in Ca and P took place, which indicates the formation of the HA-like layer. These results agree with the SEM results (Fig. 7).

Before soaking, only absorption bands shown for the ATR-FTIR spectra (Fig. 2) were under 1400 cm⁻¹ and corresponded chiefly to the silicate and phosphorous bands, which both overlapped. After soaking, the ART-FTIR spectra (Fig. 10) gave rise to new bands emerging, which corresponded to the surface product. It contains the characteristic peaks due to the vibration of the water adsorbed in apatites, a wider one at 3000-3600 cm⁻¹ and a narrower one at 1600 cm⁻¹ (see the commercial HA for similar peaks). The new precipitate presents carbonate adsorption bands at about 1450–1490 cm⁻¹ because of the partial substitution of the phosphate groups in the HA-like crystalline structure [25,26].

4. Discussion

Developing synthetic biomaterials for bone regeneration purpose is

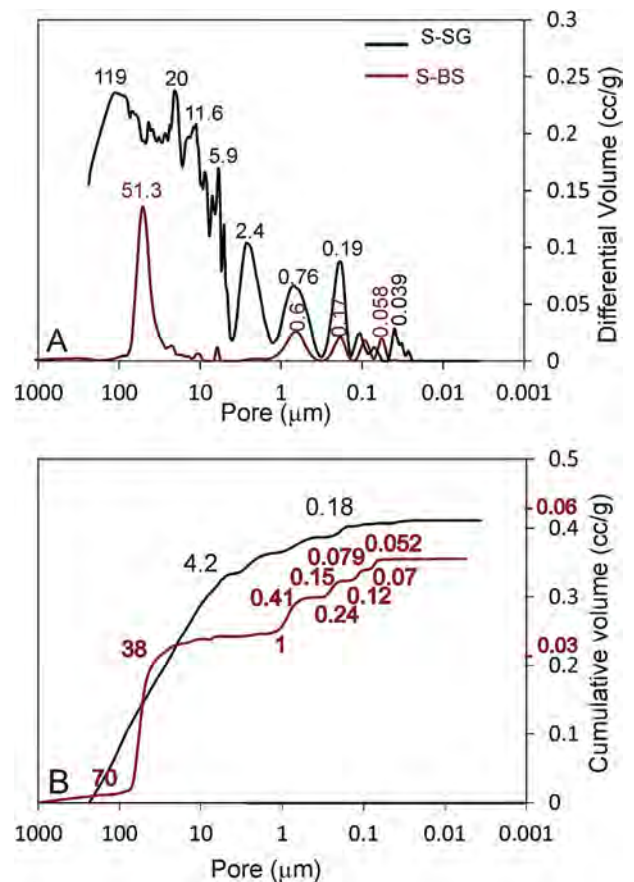


Fig. 6. Mercury intrusion curves of scaffolds S-SG scaffold (Black line) and S-BS (Red line) measured by mercury porosimetry: (A) differential volume intruded volume versus pore diameter; (B) cumulative intruded volume versus pore diameter.

demand for patients' rehabilitation. Improvements made to the structure and composition of such materials are needed for better interactions between the material and the host tissue and, hence, to achieve enhanced bone deposition [27].

This study describes the successful development of new bioactive ceramic scaffolds capable of simultaneously releasing three bioactive ions to the surrounding environment, and which are essential for conferring the signals needed for bone formation.

By controlling the processing route, we designed two scaffold ceramic materials whose nominal composition was the same (24.3 wt% SiO₂-61.65 wt% CaO-14.18 wt% P₂O₅), but with a different microstructure: the sol-gel route produced a multiphase material with high

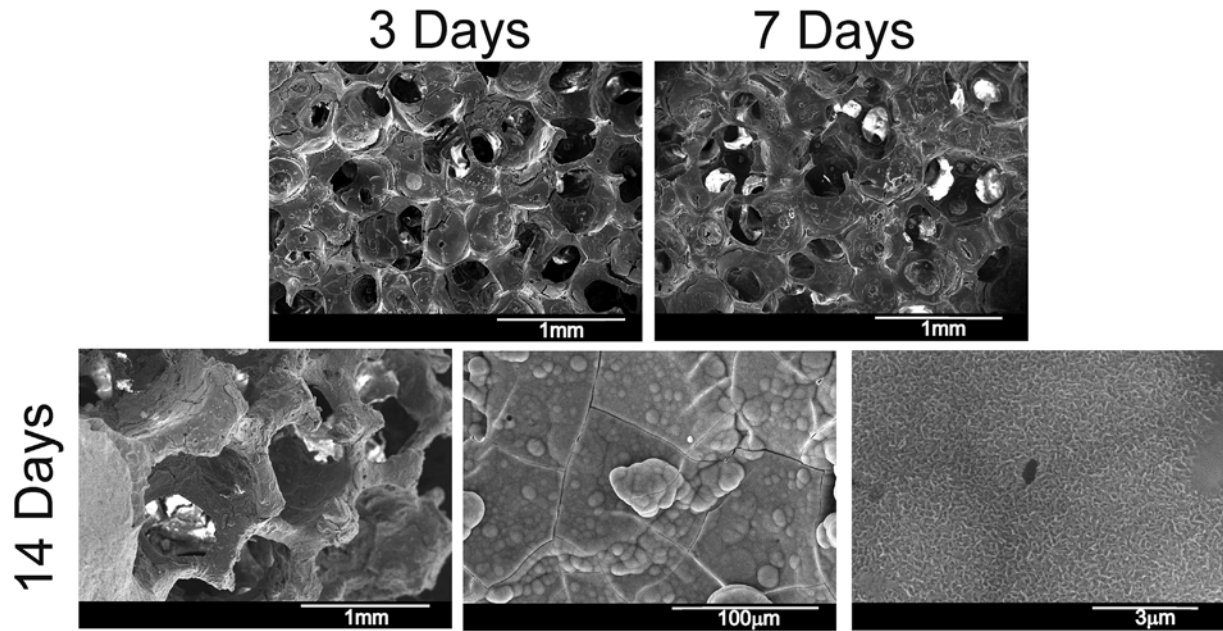


Fig. 7. SEM images of the S-SG scaffold after soaking in SBF for different times.

microporosity (Figs. 1A and 3). The ceramic slurry in the barbotine suspension processes generated a biphasic material with a lamellar morphology of calcium silicophosphate and α' -dicalcium silicate (Figs. 1B, 4 and 5), in agreement with the Alkemade line $\text{Ca}_2\text{SiO}_4 - \text{Ca}_3\text{P}_2\text{O}_8$ [3,18] contained in the $\text{SiO}_2\text{-CaO-P}_2\text{O}_5$ system.

In the S-SG scaffold, the precursors (TEOS and TEP in this study) were total or partially hydrolyzed according to acid catalysis. Two partially hydrolyzed molecules can be linked by a condensation

reaction [28]. This reaction can be extended to many molecules by the polymerization process. The bond between two monomers is made through Si–O–Si bonds for the TEOS precursor, and through P–O–P bonds for the TEP precursor. Once the ceramic has sintered, the aforementioned Si–O–Si and P–O–P bonds enhance the formation of the polymorphous phases of SiO_2 and $\text{Ca}_2\text{P}_2\text{O}_7$. Once the ceramic has sintered, the Si–O–Si bonds enhance the formation of the polymorphous phases of SiO_2 and Ca_2SiO_4 , and the P–O–P bonds enhance the

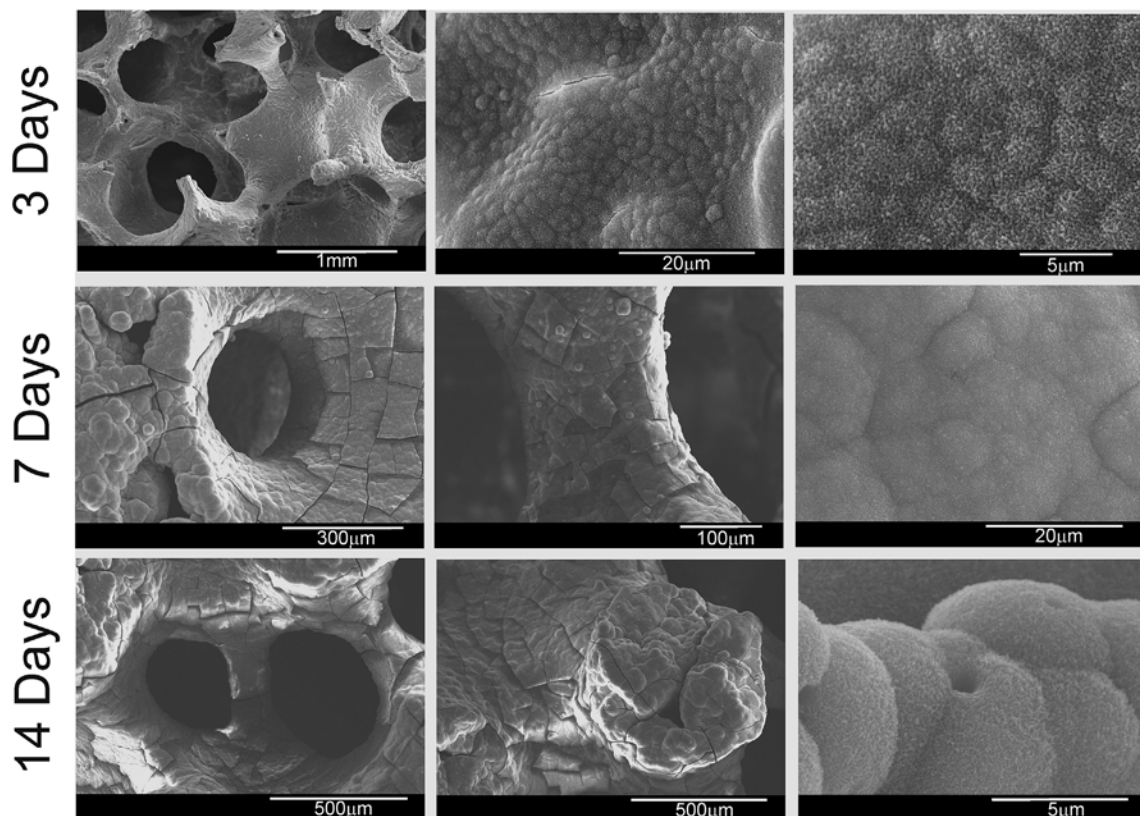


Fig. 8. SEM images of the S-BS scaffold after soaking in SBF for different times.

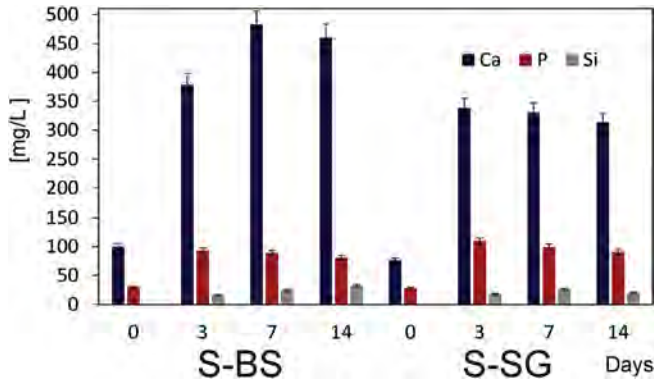


Fig. 9. Changes in the Ca, P, Si elements in the SBF after different soaking times.

formation of $\text{Ca}_3\text{P}_2\text{O}_8$ and $\text{Ca}_2\text{P}_2\text{O}_7$. This implies a deviation of Alkemade line Ca_2SiO_4 - $\text{Ca}_3\text{P}_2\text{O}_8$. S-B remains within the Alkemade line and, consequently, has only two phases (Ca_2SiO_4 and $\text{Ca}_7\text{P}_2\text{Si}_2\text{O}_{14}$) and an irregular lamellar morphology (Figs. 1B, 4 and 5).

The ATR-FTIR spectra collected for both scaffolds were dominated by the internal modes of the PO_4^{3-} and SiO_4^{4-} tetrahedral units, and showed the characteristic bonds corresponding to the inorganic and calcium silicates, and to the calcium phosphates (tricalcium phosphate, pyrophosphate) and the calcium silicophosphates phases found in XRD (Fig. 1). Given the similarities of the tetrahedral SiO_4^{4-} and PO_4^{3-} groups, a combination and the overlapping of these bands were observed. As the above-mentioned inorganic crystalline phases shared many similarly spaced vibrational modes [20–26], the spectra analysis was not easy.

The SEM microstructural analysis confirmed high interconnected porosity for the S-B and S-SG scaffolds (Figs. 3 and 4), which could improve not only uniform cell distribution and seeding, but also nutrient and metabolites diffusion. The random pore distribution was similar in both scaffolds (300–600 μm for S-B, 300–500 μm for S-SG). The small difference was because S-B was obtained after 3 immersions in the barbotine suspension, while it took 25 immersions to obtain the S-SG in the sol-solution before obtaining a scaffold with sufficient manipulability.

Apart from macroporosity information, mercury porosimetry was performed to collect information about the microporosity in the scaffolds (Table 2). The micropores on the macropore surface considerably increased the surface area of the potential implant. S-SG displayed greater interparticle porosity (39.66%) compared to S-B (8.76%),

which implies a large surface area (1.19 m^2/g for S-SG versus 0.36 m^2/g for S-B) for the scaffolds obtained by means of interconnected porosity and allows a better bone-scaffold interaction.

Despite some disagreements about the ideal pore size, it has been well-established that pores below 10 μm provide a larger surface area for the implant-natural bone interaction, which adds protein adsorption, ion exchange and new bone formation [29,30], while pores around 100 μm enhance osteoblast initial adhesion and allow their migration to the biomaterial [6,13]. However, bigger pores (> 300 μm) are needed to also improve new bone formation [11,12]. Depending on specific needs, a balanced combination of macro- and micropores should be custom-made for cell penetration and protein adsorption purposes [29–31].

The results of Table 2 confirmed a network porosity of 48.9% for S-SG and of 12.83% for S-B, as well as differences in intra- and interparticle porosity. However, it is worth bearing in mind that the mercury porosimetry technique is more suitable for intra- and interparticle pore analysis, with the upper detection limit of the technique being 300 μm . In fact part of the porosity observed by SEM is not herein presented. Macroporosity was studied by the Archimedes method in H_2O (10 samples per scaffold) given a high porosity of up to ~95% in both scaffolds.

The swallowing shown in Fig. 4B of the S-B scaffold ceramic sintered at 1550 $^\circ\text{C}$ could be to the formation of a low-viscosity calcium-silicophosphate liquid that penetrated the open pores by capillarity, and led them to close, as observed by the large round pores presented in the microstructure. An ultrastructural analysis was done by FESEM to obtain a better resolution (Fig. 5A), where these lamellae also presented a roughness topography due to grain sintering. Surface textures, apart from porosity, favor adhesion and cells spreading, which improve bioactivity and tissue regeneration [6,17,18]. The lamellar structure was assumed to be composed of alternative lamellae of dicalcium silicate and calcium silicophosphate. Although several chemical etching times and dissolutions were studied, only one lamella was identified. The EDS composition analysis of this lamella confirmed that it did not correspond to any of the phases initially present in the material. The dicalcium silicate phase degraded because of acid etching, and calcium silicophosphate appeared as a phosphorous-deficient calcium silicophosphate, as seen in the EDS analysis by making a comparison with that corresponding to the single-phase calcium silicophosphate (Fig. 5B and C).

Both scaffolds, compared to other scaffolds made by different routes [31–33], were weaker, which made their handling more difficult. For this reason, 25 PU immersions were performed in the sol-solution, with three in the barbotine suspension, which did not compromise the

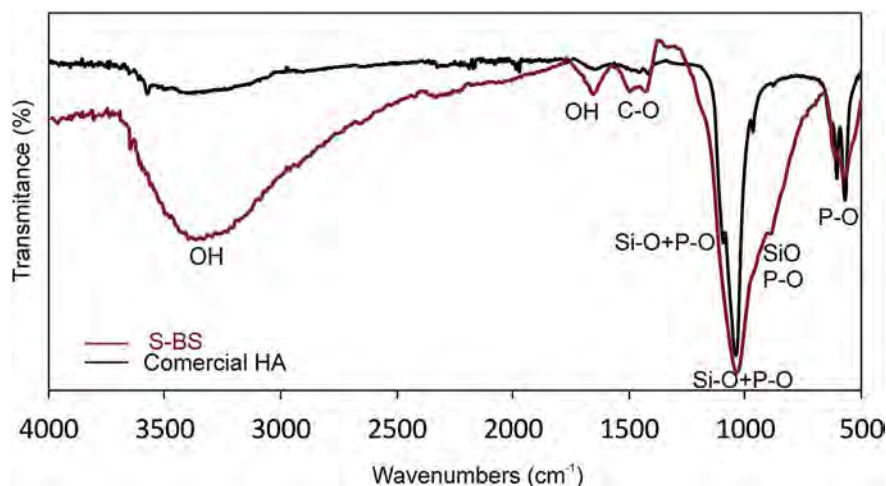


Fig. 10. ATR-FTIR spectra of the precipitated layer on scaffold S-B after 21 days of immersion in SBF, representative of both scaffolds, and the commercial HA for comparison purposes.

densification process. During this process, the ceramic structure was strengthened via atomic diffusion mechanisms, and depended directly on both temperature and sintering time. Therefore, the thermal stability of the developed scaffolds was good and, thus, resulted in a much denser and stronger microstructure.

The role played by ceramic scaffolds aims to create space for osteoblasts to grow, adhere and proliferate, and to supply channels in order to transport nutrients and metabolic waste while diseased or damaged bone is repaired [6,11,12,28–30]. Based on the above results, evidently both scaffold materials displayed excellent *in vitro* bioactive behavior when immersed in SBF. Both scaffolds were bioactive, but differently.

In relation to S-BS, the changes recorded in the Si, Ca and P ion concentrations (Fig. 9- S-BS) showed that when soaking began, the scaffold released the three ions to the medium. The Si concentration continuously rose throughout the experiment to reach 32 mg/L after 14 days of soaking. This means that the phase that was or the phases that were dissolving contained a high Si content. Therefore, they will be α' -H-dicalcium silicate and/or calcium silicophosphate. In the second soaking step, the concentration of the Ca ions in SBF lowered to 460 mg/L due to the precipitation of the HA layer that coated the scaffold surface (Fig. 8). The P concentration also lowered to 80 mg/L over 14 days.

We think that the first phase during dissolving was α' -H-dicalcium silicate with the release of Ca^{2+} and HSiO_4^{3-} , and due to increasing the activities of these ions in the neighborhood of the reacting scaffold surface until they exceeded the solubility product of HA. With the release of the Ca^{2+} ions from α' -H-dicalcium silicate, many Si-OH groups formed on the surfaces of S-BS. These silanol groups induced the heterogeneous nucleation of apatite, and the released Ca^{2+} ions increased the ionic activity product of apatite by enhancing apatite nucleation. The partial dissolution of calcium silicophosphate in SBF also occurred with the release of SiO_4^{4-} , HPO_4^{2-} and Ca^{2+} .

Next the nucleation of an HA layer took place on the scaffold's surface by the reaction of the HPO_4^{2-} ions with the excess of Ca^{2+} ions released to SBF by the partial dissolution of the calcium silicophosphate phase. Once apatite nuclei had formed on the scaffold's surface, they were able to grow spontaneously by consuming the calcium and phosphate ions from the surrounding SBF solution.

In relation to the scaffold made by the sol-gel method, the Si, Ca, and P ion concentrations in SBF (Fig. 9- S-SG) showed that when soaking began, S-SG released the three ions to the medium in a much smaller proportion than S-BS. The first HA precipitate was found after the scaffold had been soaked in SBF for 14 days (Fig. 7). Thus S-SG bioactivity drastically decreased compared to S-BS, where the first HA precipitation took place after 3 days of soaking. Furthermore, given the precipitation kinetics, clear differences were found in the geometrics of the obtained precipitate. As seen in S-SG (Fig. 7), the surface was covered by a homogeneous spherulitic-shaped layer that joined together and was formed by tiny worm-like crystals. S-BS presented cauliflower particles which, with time, joined and formed a large dense layer of smooth spheres (Fig. 8.)

Although S-SG had a bigger surface area (Fig. 3C and Table 2 part II) than S-BS, and as bioactivity should be theoretically faster, the presence of pyrophosphate ($\text{Ca}_2\text{P}_2\text{O}_7$) delayed the appearance of HA. It is well-known that low inorganic pyrophosphate concentrations inhibit not only the growth, but also the precipitation, of hydroxyapatite crystals *in vitro* and *in vivo* [34–36]. Bone is renewed constantly by balanced osteoblastic bone formation and osteoclastic bone resorption activities. This bone remodeling process is relevant for achieving not only normal bone mass and strength, but also mineral homeostasis. Body fluids are supersaturated in relation to phosphate and calcium, whereas the presence of nucleating agents facilitates mineralization. Collagen is a major nucleator, and supersaturated phosphate and calcium levels were maintained by the presence of inhibitors. Pyrophosphate inhibitory actions have been widely studied in bone. Today it is believed that the

phosphate-to-pyrophosphate ratio is a fundamental regulator of skeletal mineralization in the bone microenvironment [37]. Accordingly, pyrophosphate is an essential molecule for the remodeling of bone tissue. This molecule plays an important role by inhibiting the crystallization of hydroxyapatite in connective tissue, the urinary tract and other extracellular fluids [37,38].

In addition, bone regeneration can be done using active compounds like pyrophosphates because they are able to promote osteoblast proliferation and differentiation when inhibiting osteoclast genesis *in vitro* [39]. Despite the exact biological role that silicon plays in bone health remaining unclear, it benefits bone health by playing a key role in bone homeostasis and regeneration and, hence, represents a potential trace element to treat and prevent bone diseases like osteoporosis.

Our objective was to compare two materials with the same nominal composition that were obtained by different methods. Only S-BS had a lamellar microstructure, which remained after the heat treatment in the Alkemade line $\text{Ca}_2\text{SiO}_4 - \text{Ca}_3\text{P}_2\text{O}_8$. So the scaffolds with a lamellar microstructure, and composed of two phases of different degradation rates, would be an excellent starting point to develop third-generation biomaterials. Thus interconnectivity, pore size, pore distribution and porosity level need to be balanced to guide proper tissue ingrowth, and a balance must be struck with scaffold degradation as it must provide mechanical support during regeneration. To our knowledge, this is the first study about porous scaffolds with a eutectoid composition.

5. Conclusions

With the system $\text{SiO}_2\text{-CaO-P}_2\text{O}_5$, we designed and processed two materials with a chemical composition of the invariant eutectoid point and different structures (a single polycrystalline or lamellar morphology). The combination of structural, chemical and morphological factors was responsible for the various *in vitro* behaviors displayed by the two materials, and shared a common composition. Our results confirm that not only the physiological medium has to be properly selected, but also the materials' chemical composition, structure and microstructure have to be studied in-depth to determine a given material's *in vitro* potential bioactivity.

Acknowledgments

Part of this work has been supported by Ministry of Economy and Competitiveness (MINECO) contract grant number: MAT2013-48426-C2-2-R.

References

- [1] S. Serena, M.A. Sainz, A. Caballero, Single-phase silicocarnotite synthesis in the subsystem $\text{Ca}_3(\text{PO}_4)_2\text{-Ca}_2\text{SiO}_4$, *Ceram. Int.* 40 (6) (2014) 8245–8252, <https://doi.org/10.1016/j.ceramint.2014.01.022>.
- [2] G.J. Lugo, P. Mazón, P.N. De Aza, Material processing of a new calcium silicophosphate ceramic, *Ceram. Int.* 42 (2016) 673–680, <https://doi.org/10.1016/j.ceramint.2015.08.164>.
- [3] V. Rubio, M.A. De la Casa-Lillo, S. De Aza, P.N. De Aza, The system $\text{Ca}_2\text{SiO}_4\text{-Ca}_3(\text{PO}_4)_2$: the subsystem $\text{Ca}_2\text{SiO}_4\text{-7CaOP}_2\text{O}_4\text{2SiO}_2$, *J. Am. Ceram. Soc.* 94 (2011) 4459–4462, <https://doi.org/10.1111/j.1551-2916.2011.04716.x>.
- [4] P. Velasquez, Z.B. Luklinska, L. Meseguer-Olmo, J.E. Mate-Sanchez de Val, R.A. Delgado-Ruiz, J.L. Calvo-Guirado, MaP. Ramirez-Fernandez, P.N. de Aza, α -TCP ceramic doped with dicalcium silicate for bone regeneration applications prepared by powder metallurgy method: *in vitro* and *in vivo* studies, *J. Biomed. Mater. Res. A* 101 (7) (2013) 1943–1954, <https://doi.org/10.1002/jbm.a.34495>.
- [5] G. Criscenti, A. Longoni, A. Di Luca, C. De Maria, C.A. Van Blitterswijk, G. Vozzi, L. Moroni, Triphasic scaffolds for the regeneration of the bone-ligament interface, *Biofabrication* 8 (1) (2016) 015009, <https://doi.org/10.1088/1758-5090/8/1/015009>.
- [6] R. Rabadan-Ros, P. Velásquez, L. Meseguer-Olmo, P.N. De Aza, Morphological and structural study of a novel porous Nurse's A ceramic with osteoconductive properties for tissue engineering, *Materials* 9 (6) (2016) 474, <https://doi.org/10.3390/ma9060474>.
- [7] A. Olad, F.F. Azhar, The synergistic effect of bioactive ceramic and nanoclay on the properties of chitosan-gelatin/nanohydroxyapatite-montmorillonite scaffold for bone tissue engineering, *Ceram. Int.* 40 (2014) 10061–10072, <https://doi.org/10.1016/j.ceramint.2014.01.022>.

- 1016/j.ceramint.2014.04.010.
- [8] P. Ros-Tárraga, A. Murciano, P. Mazón, S. A Gehrke, P.N. De Aza, New 3D stratified Si-Ca-P porous scaffolds obtained by sol-gel and polymer replica method: microstructural, mineralogical and chemical characterization, *Ceram. Int.* 43 (8) (2017) 6548–6553, <https://doi.org/10.1016/j.ceramint.2017.02.081>.
- [9] P. Mazon, P.N. De Aza, Porous scaffold prepared from α -L-Dicalcium silicate doped with phosphorus for bone graft, *Ceram. Int.* 44 (1) (2018) 537–545, <https://doi.org/10.1016/j.ceramint.2017.09.208>.
- [10] S. Mondal, G. Hoang, P. Manivasagan, M.S. Moorthy, T.P. Nguyen, T.T. Vy Phan, H.H. Kim, M.H. Kim, S.Y. Nam, J. Oh, Nano-hydroxyapatite bioactive glass composite scaffold with enhanced mechanical and biological performance for tissue engineering application, *Ceram. Int.* 44 (13) (2018) 15735–15746, <https://doi.org/10.1016/j.ceramint.2018.05.248>.
- [11] A. Parrilla-Almansa, N. García-Carrillo, P. Ros-Tárraga, C.M. Martínez, F. Martínez-Martínez, L. Meseguer-Olmo, P.N. de Aza, Demineralized bone matrix coating Si-Ca-P ceramic does not improve the osseointegration of the, *Scaffold Mater.* 11 (2018) 1580, <https://doi.org/10.3390/ma11091580>.
- [12] P.N. De Aza, M.A. Rodríguez, S.A. Gehrke, J.E. Maté-Sánchez de Val, J.L. Calvo-Guirado, A Si- α TCP scaffold for biomedical applications: an experimental study using the rabbit tibia model, *Applied Sciences-basel* 7 (2017) 706, <https://doi.org/10.3390/app7070706>.
- [13] O. Gauthier, J.M. Bouler, E. Aguado, P. Pilet, G. Daculsi, Macroporous biphasic calcium phosphate ceramics: influence of macropore diameter and macroporosity percentage on bone ingrowth, *Biomaterials* 19 (1998) 133–139.
- [14] S. Ramezani, R. Emadi, M. Kharaziha, F. Tavangarian, Synthesis, characterization and in vitro behavior of nanostructured diopside/biphasic calcium phosphate scaffolds, *Mat. Chem. Phys.* 186 (2017) 415–425.
- [15] P.N. De Aza, Z. B Luklinska, M. Anseau, F. Guitian, S. De Aza, Electron microscopy of interfaces in a wollastonite-tricalcium phosphate bioeutectic material, *J. Microsc.* 189 (2) (1998) 145–153, <https://doi.org/10.1046/j.1365-2818.1998.00286.x>.
- [16] P.N. De Aza, S. Serena, Z. B Luklinska, Manufacture and characterization of a new Si-Ca-P biphasic ceramic, *Ceram. Int.* 44 (12) (2018) 13623–13629, <https://doi.org/10.1016/j.ceramint.2018.04.198>.
- [17] A.H. De Aza, P. Velasquez, M.I. Alemany, P. Pena, P.N. De Aza, In situ bone-like apatite formation from a Bioeutectic® ceramic in SBF dynamic flow, *J. Am. Ceram. Soc.* 90 (4) (2007) 1200–1207, <https://doi.org/10.1016/j.noncrysol.2005.04.062>.
- [18] V. Rubio, P. Mazón, M.A. de la Casa-Lillo, P.N. De Aza, Preparation, characterization and in vitro behaviour of a new eutectoid bioceramics, *J. Eur. Ceram. Soc.* 35 (1) (2015) 317–328, <https://doi.org/10.1016/j.jeurceramsoc.2014.08.039>.
- [19] T. Kokubo, H. Takadama, How useful is SBF in predicting in vivo bone bioactivity? *Biomaterials* 27 (2006) 2907–2915, <https://doi.org/10.1016/j.biomaterials.2006.01.017>.
- [20] H. Aguiar, J. Serra, P. González, B. León, Structural study of sol-gel silicate glasses by IR and Raman spectroscopies, *J. Non-Cryst. Solids* 355 (2009) 475–480.
- [21] A. Meiszterics, L. Rosta, H. Peterlik, J. Rohonczy, S. Kubuki, P. Henits, K. Sinko, Structural characterization of gel-derived calcium silicate systems, *J. Phys. Chem. A* 114 (2010) 10403–10411.
- [22] A. Gozalian, A. Behnamghader, M. Daliri, A. Moshkforoush, Synthesis and thermal behavior of Mg-doped calcium phosphate nanopowders via the sol gel method, *Sci. Iran.* 18 (2011) 1614–1622.
- [23] P. Innocenzi, Infrared spectroscopy of sol-gel derived silica-based films: a spectro-microstructure overview, *J. Non-Cryst. Solids* 316 (2003) 309–319.
- [24] G. Apsana, P.P. George, N. Devanna, Facile green synthesis and characterization of calcium pyrophosphate nanoparticles using D- Glucose, *Mater. Today: Proceedings* 4 (2017) 10913–10920.
- [25] F. Ren, Y. Ding, Y. Leng, Infrared spectroscopic characterization of carbonated apatite: a combined experimental and computational study, *J. Biomed. Mater. Res. A* 102 (2014) 496–505.
- [26] A.P. Solonenko, A.I. Blesman, D. Polonyankin, Preparation and in vitro apatite-forming ability of hydroxyapatite and β -wollastonite composite materials, *Ceram. Int.* Volume 44 (15) (2018) 17824–17834, <https://doi.org/10.1016/j.ceramint.2018.06.251>.
- [27] A.J. Salinas, P. Esbrit, M. Vallet-Regí, A tissue engineering approach based on the use of bioceramics for bone repair, *Biomater. Sci.* 1 (2013) 40–51, <https://doi.org/10.1039/c2bm00071g>.
- [28] I. Bruzauskaitė I, D. Bironaitė, E. Bagdonas, E. Bernotienė, Scaffolds and cells for tissue regeneration: different scaffold pore sizes-different cell effects, *Cytotechnology* 68 (2016) 355–369.
- [29] F.S.L. Bobbert, A.A. Zadpoor, Effects of bone substitute architecture and surface properties on cell response, angiogenesis, and structure of new bone, *J. Mater. Chem. B* 5 (31) (2017) 6175–6192.
- [30] C.M. Murphy, M.G. Haugh, F.G. O'Brien, The effect of mean pore size on cell attachment, proliferation and migration in collagen-glycosaminoglycan scaffolds for bone tissue engineering, *Biomaterials* 31 (2010) 461–466.
- [31] N. Sachot, O. Castano, J.A. Planell, E. Engel, Optimization of blend parameters for the fabrication of polycaprolactone-silicon based ormoglass nanofibers by electrospinning, *J. Biomed. Mater. Res. Part B* 103 (6) (2015) 1287–1293, <https://doi.org/10.1002/jbm.b.33306>.
- [32] A. Wubneh, E.K. Tsekoura, C. Ayranci, H. Uludağ, Current state of fabrication technologies and materials for bone tissue engineering, *Acta Biomater.* 80 (2018) 1–30, <https://doi.org/10.1016/j.actbio.2018.09.031>.
- [33] C.G. De Paula, E.S. Trichês, Preparation and characterization of β -tricalcium phosphate scaffolds by freeze casting method, *Ceramica* 64 (372) (2018) 553–558, <https://doi.org/10.1590/0366-69132018643722415>.
- [34] H. Fleisch, S. Bisaz, Mechanism of calcification: inhibitory role of pyrophosphate, *Nature* 195 (1962) 911.
- [35] H. Fleisch, R.G.G. Russell, F. Straumann, Effect of pyrophosphate on hidroxiapatite and its implications in calcium homeostasis, *Nature* 212 (26) (1966) 901–903.
- [36] R.A. Terkeltaub, Inorganic pyrophosphate generation and disposition in pathophysiology, *Am. J. Physiol. Cell Physiol.* 281 (2001) C1–C11.
- [37] R. Orriss, T.R. Arnett, R. Graham, G. Russell, Pyrophosphate: a key inhibitor of mineralization, *Curr. Opin. Pharmacol.* 28 (2016) 57–68, <https://doi.org/10.1016/j.coph.2016.03.003>.
- [38] J.L. Millan, The role of phosphatases in the initiation of skeletal mineralization, *Calcif. Tissue Int.* 93 (2013) 299–306.
- [39] R.E. Wuthier, S. Bisaz, R.G. Russell, H. Fleisch, Relationship between pyrophosphate, amorphous calcium phosphate and other factors in the sequence of calcification in vivo, *Calcif. Tissue Res.* 10 (1972) 198–206.